Tau, amyloid-beta and alpha-synuclein co-pathologies synergistically enhance neuroinflammation and neuropathology

Jhodi M. Webster[1, 2], Ya-Ting Yang[1, 2], Aidan T. Miller[1], Asta Zane[1], Kasandra Scholz[1], William J. Stone[1], Nikhita Mudium[1], Nicole J. Corbin-Stein[1,2], Woong-Jai Won[1], Anna C. Stoll[1], Kelsey M. Greathouse[1], Noelle H. Cooper[1], Lillian F. Long[1], Phaedra N. Manuel[1], Jeremy H. Herskowitz[1], Talene A. Yacoubian[1], Daniel J. Tyrrell[3], Ivette M. Sandoval[5], Fredric P. Manfredsson[2, 5], Jeffrey H. Kordower[2,6], and Ashley S. Harms[1, 2]*

Author affiliations:

[1]University of Alabama at Birmingham, Department of Neurology, Killion Center for Neurodegeneration and Experimental Therapeutics, Birmingham, AL, 35294

[2]Aligning Science Across Parkinson's (ASAP) Collaborative Research Network, Chevy Chase, MD, 20815

[3]University of Alabama at Birmingham, Department of Pathology, Division of Molecular and Cellular Pathology, Birmingham, AL, 35294

[4]Neurodegenerative Diseases Research Unit, Biogen, Cambridge, MA, 02142

[5]Barrow Neurological Institute, Department of Translational Neuroscience; Phoenix, AZ, 85013

[6]Arizona State University, ASU-Banner Neurodegenerative Disease Research Center, Bio-design Institute, Tempe, AZ, 85281

***Correspondence to:**

Ashley S. Harms

University of Alabama at Birmingham, 1719 6th Ave South, Birmingham, Alabama 35294

anharms@uab.edu

Running title: Co-pathologies drive neuroinflammation in disease

Keywords: co-pathologies, neuroinflammation, α-synuclein, tau, amyloid beta, T cells, microglia

Abstract

Alzheimer's and Parkinson disease pathology often co-occur, with amyloid-β and phosphorylated tau, found in 30-50% of idiopathic Parkinson disease cases. α -synuclein inclusions, a hallmark of Parkinson disease, are present in 50% of Alzheimer's cases and the co-expression of these pathologies is linked to faster cognitive decline and earlier death. Immune activation is a hallmark of both diseases, but current model systems primarily examine each pathology in isolation. As such, how these co-pathologies interact to drive inflammation and neuronal loss remain poorly understood. To address this, we developed a co-pathology mouse model combining tau, amyloid-β, and α-synuclein. Here, we show that co-pathologies synergistically trigger a distinct and amplified neuroimmune response, marked by robust expansion of $CD4^+$ and $CD8^+$ tissue-resident memory T cells and increased $CD68^+$ microglia, a population of activated, phagocytosing microglia, compared to single pathology brains. These changes were abundant in the hippocampus and cortex, regions showing elevated amyloid-β protein pathology load and enhanced neuronal loss with co-pathology expression. Our findings demonstrate that co-pathologies act synergistically to enhance immune activation prior to neurodegeneration. This model provides a platform for assessing mixed-pathology mechanisms and identifies key immune cell populations that may drive disease acceleration across Alzheimer's, Parkinson disease and their related dementias.

43 # Introduction

44 In addition to the progressive loss of neurons and brain atrophy, neurodegenerative diseases
45 share the common feature of pathogenic protein accumulation and worsening cognitive decline.
46 These proteins include α-synuclein (α-syn) inclusions found in Lewy bodies and Lewy neurites in
47 Parkinson disease (PD) and Parkinson disease dementia (PDD), extracellular amyloid-β (Aβ)
48 plaques and phosphorylated-tau (tau) tangles in the form of intracellular neurofibrillary tangles in
49 Alzheimer's disease (AD) [1-3]. Although these proteins are pathologically associated with their
50 respective diseases, there is evidence for the overlap of pathology and symptoms. The presence of
51 these AD-related pathologies, found in 50-80% of PD brains [4-11], has been a significant contributor
52 to exacerbated disease progression and dementia onset in patients with PD [9,12]. Similarly, Lewy
53 bodies have been found in the brains of AD patients[13,14] and more recently, a-syn co-pathology has
54 been shown to promote amyloid-driven tau accumulation in AD brains[15]. The co-expression of
55 these pathologies has been linked to worsened cognitive decline and higher rate of mortality[16-19].
56 This exacerbated disease phenotype under co-pathology conditions suggests potential synergy
57 between α-syn, tau and Aβ, however the disease-progressing mechanisms of this co-expression
58 remain unknown.

59 Previously, co-pathology mouse models have also implicated potential interactions
60 between pathologies. In dementia with Lewy body (DLB)-AD and PD-AD mouse models,
61 combined tau, Aβ and α-syn pathologies enhanced aggregation and spreading of pathology beyond
62 single pathology effects[20-22]. Neurodegeneration, however, was only shown to be influenced by
63 Aβ and α-syn co-pathology in 5XFAD mice injected with α-syn mouse pre-formed fibrils (PFFs)
64 [20]. Additionally, neuroinflammation in the presence of the co-pathologies was not fully assessed
65 in these animal models. As such, it remains unknown how these co-pathologies may promote the

66 immune cell activation leading to the neurodegeneration and sustained aggregated protein
67 pathology seen in human disease.

68 Neuroinflammation, driven by microglia and CNS-resident macrophages, infiltrating
69 lymphocytes, and monocytes, is a key contributor to neuronal loss and neurodegenerative disease
70 progression. $CD4^+$ and $CD8^+$ T cells are found in the brains and cerebrospinal fluid [23] of AD [24-27],
71 PD [28-30], and DLB patients along with activation of myeloid cells, including microglia,
72 macrophages and monocytes. In AD, Aβ plaques trigger and can interact with microglia to adopt
73 a phagocytic but dysfunctional disease-associated microglia phenotype[31,32] while Aβ-specific T
74 cells infiltrate the brain and exacerbate tau pathology and neurodegeneration[33]. Tau pathology also
75 triggers a pro-inflammatory phenotype in microglia through receptor binding[34] and promotes CNS-
76 specific changes in T cell reactivity[35]. In PD, α-syn interacts with toll-like receptors (TLRs) on
77 microglia to promote release of inflammatory cytokines[36], while T cells target α-syn epitopes in
78 the substantia nigra pars compacta (SNpc) [37,38]. While these cells aid in immune surveillance
79 during homeostatic conditions, in chronic disease, microglia and T cells may adopt pro-
80 inflammatory phenotypes and contribute to neurotoxicity and exacerbated neuronal damage[39-43].
81 How combined tau, Aβ and α-syn pathologies synergistically amplify immune activation remains
82 unclear.

83 To further understand how co-pathologies drive neurodegeneration, we aimed to determine
84 whether the combined presence of tau, Aβ and α-syn promotes neuroinflammation, protein
85 aggregation and neuronal loss through synergistic effects. To do this, we developed a co-pathology
86 mouse model, generated by injection of adeno-associated virus (AAV)-double mutant tau into the
87 entorhinal cortex and α-syn mouse PFFs into the striatum of J20 amyloid over-expressing
88 transgenic mice[44]. This model allowed us to evaluate the impact of multiple pathological proteins

89 on innate and adaptive immune responses as well as neurodegeneration within vulnerable regions,
90 including the hippocampus. We found that the presence of co-pathologies not only promotes
91 pathology deposition compared to single pathology models, but also triggered synergistic
92 neuroinflammatory responses and enhanced neuronal loss in the hippocampus. These findings
93 support human data[45] and model tau, Aβ and α-syn synergize to accelerate key immunopathogenic
94 processes that may contribute to neurodegenerative disease progression.
95

96 # Results

97 **Co-pathologies enhance Aβ plaques and α-syn inclusions**

98 The co-expression of tau, Aβ and α-syn has been reported in the limbic and cortical regions,
99 particularly in the hippocampus and neocortex in human postmortem studies from DLB, AD and
100 PDD brains[46-48]. To model this *in vivo* in mice, we generated a co-pathology model incorporating
101 tau, Aβ and α-syn and compared data obtained in the co-pathology model with mice only
102 expressing a single pathology. As a tau single pathology control, tau pathology was induced in
103 non-transgenic (NTG), C57BL/6J mice via bilateral entorhinal cortex injection of an AAV
104 expressing human tau with two mutations (AAV9-Tau) (Figure 1a). To model Aβ single
105 pathology, J20 transgenic (Tg) mice[44], which overexpress human mutant amyloid precursor
106 protein (APP^{mut}) and develop Aβ plaques in the hippocampus and cortex (Figure 1b), were aged
107 to 6 months old. Lastly, for α-syn single pathology control, 12–14-week-old NTG mice received
108 bilateral injections of mouse α-syn PFFs into the dorsal lateral striatum (Figure 1c). To create a
109 model of co-pathology, age-matched J20 mice were bilaterally injected with both α-syn PFFs into
110 the basal lateral striatum and AAV9-Tau into the entorhinal cortex during one stereotaxic surgery

111 session, combining tau, Aβ and α-syn pathologies in one model (Figure 1d) resulting in co-
112 pathologies in the hippocampus and cortex.
113
114 Co-pathologies exhibit synergistic interactions that promote the aggregation and accumulation of
115 disease-associated protein[10,15,49,50]. To determine whether the presence of co-pathology enhances
116 α-syn, tau and Aβ individually, single pathology controls and co-pathology brains were assessed
117 for histological and biochemical markers of protein pathology at 3 months post-induction (mpi)
118 using immunohistochemistry (IHC), western blotting, and enzyme linked immunosorbent assay
119 (ELISA) (Figure 2a). AT-8^{+} neurons were immunolabeled in the cortex and hippocampus of 6-
120 month-old (3mpi) Tau single pathology and co-pathology mice (Figure 2b). Total tau protein
121 expression was assessed using western blot, showing no major changes in total tau expression
122 between co-pathology mice and Tau single pathology controls (Figure 2c). A decrease in soluble
123 tau in the cortex of co-pathology mice (Figure 2d) was observed. Using an antibody specific to Aβ
124 aggregation, Aβ^{+} plaques were also observed in the cortex and hippocampus (Figure 2e), with
125 increased deposition of Triton X-100 insoluble $A\beta_{1-42}$ load in the hippocampus of co-pathology
126 mice, as assessed by ELISA (Figure 2f). pSer129^{+} α-syn inclusions were also visible within the
127 neurites and cell bodies in the cortex and hippocampus of α-syn single pathology and co-pathology
128 mice (Figure 2g). Western blot analysis showed increase in soluble total α-syn levels in the cortex
129 of co-pathology brains compared to α-syn single pathology controls (Figure 2h,i). Uncropped
130 Western blots are shown within Extended Data Figure 1. These results indicate enhanced
131 hippocampal and cortical insoluble Aβ and soluble α-syn pathology load in a co-pathology
132 environment beginning at 3mpi.
133

134 **Neuronal loss is driven by the co-expression of tau, Aβ and α-syn pathologies**

135 Neurodegeneration, including changes in synaptic density and the subsequent death of neurons,
136 occurs prior to severe onset of symptoms associated with neurodegenerative diseases. Such
137 symptoms include cognitive and motor impairments [51-54]. Given the involvement of tau, Aβ and
138 α-syn in neurodegenerative diseases strongly associated with cognitive impairment, we performed
139 open field, Barnes maze, rotarod and pole behavioral tests to assess for cognitive and motor deficits
140 in the model at 6mpi (Extended Data Figure 2). Sham mice, NTG animals bilaterally injected with
141 α-syn monomer and AAV9-GFP into the striatum and entorhinal cortex, respectively, were used
142 as a surgical control for co-pathology mice. Behavioral changes were observed with co-pathology
143 mice making significantly more errors and reduced time to commit errors compared to sham mice,
144 but no significant difference was observed when compared to single pathology controls (Extended
145 Data Figure 2). Co-pathology mice showed increased turnaround and total time on the pole test
146 compared to Sham mice (Extended Data Figure 2b). The open field test only showed increased
147 distance traveled by the co-pathology mice compared to sham (Extended Data Figure 2c).
148 However, overall co-pathology mice showed no differences in movement as shown by the rotarod
149 test (Extended Data Figure 2d). In summary, co-pathologies did not produce any synergistic effects
150 on motor or cognitive function in mice. This may be due to the intrinsic neural hyperexcitability
151 of the J20 mouse model, which is known to drive a hyperactive behavioral phenotype[55,56].

152 Dendritic spine morphology is an indicator of synaptic integrity and plasticity, both of which are
153 disrupted in neurodegenerative diseases associated with cognitive decline[57-59]. To test the
154 hypothesis that tau, Aβ and α-syn co-pathologies synergize to exacerbate synaptic dysfunction, we
155 performed a detailed morphometric analysis of dendritic spines on Lucifer yellow labelled CA1
156 pyramidal neurons in the hippocampus across single and co-pathology brains. Our analysis

157 revealed that while the number of total spines remained unchanged across groups, co-pathologies
158 resulted in significantly shorter total spine length in the hippocampus compared to α-syn alone
159 (Extended Data Figure 3a). Additionally, the length of thin spines on apical dendrites was
160 decreased in the hippocampus of co-pathology mice, suggesting increased structural instability
161 that could impair synaptic function (Extended Data Figure 3b). Finally, spine volume on basal
162 dendrites was reduced in the hippocampus of co-pathology mice relative to brains with only Aβ or
163 α-syn pathology, which could indicate diminished postsynaptic density (Extended Data Figure 3c).
164 Collectively, these findings point to synergistic interactions of co-pathologies that drive distinct
165 changes in synaptic morphology, which may represent a mechanism that promotes neuronal loss
166 in this brain region.

167 Neuronal loss is a hallmark feature observed in both AD and PD, with region-specific vulnerability
168 depending on disease pathology[60-63]. Previous work, however, has only assessed neuronal loss in
169 the context of α-syn and Aβ as co-pathologies[21]. Given this and our synaptic morphology findings,
170 we next hypothesized that co-expression of tau, Aβ and α-syn may enhance neuronal loss in the
171 hippocampus. To assess neurodegeneration, we performed unbiased stereology on co-pathology
172 and single pathology controls at 6mpi (Figure 3a). We found enhanced loss (20-30%, $p<0.001$) of
173 $NeuN^+$ neurons in the CA1 region of the hippocampus in the co-pathology mice compared to tau,
174 Aβ or α-syn single pathology mice (Figure 3b,c). Within the CA3, co-pathology mice showed
175 significant loss (20-25%, $p<0.01$) compared to single tau and α-syn controls only (Figure 3d).
176 Along with cognitive decline, patients with neurodegenerative disease also exhibit significant
177 motor deficits, mostly due to the loss of neurons in motor-related cortical regions or dopaminergic
178 neurons in the SNpc[51,64]. In the SNpc at 6mpi, the loss of tyrosine hydroxylase (TH)-positive
179 neurons significantly enhanced in the co-pathology model compared to that in the Aβ single-

180 pathology animals. However, in comparison to tau and α-syn mice, the co-pathologies did not
181 enhance TH+ cell loss (Extended Data Figure 4c,d). Taken together, these results highlight a
182 synergistic interaction between tau, Aβ and α-syn co-pathologies that exacerbates
183 neurodegeneration in the hippocampus, a brain region associated with enhanced accumulation and
184 expression of protein co-pathology in human, resulting in cognitive deficits.

185

186 **Co-pathologies enhance microglial activation and infiltration of peripheral monocytes**

187 Given that tau, Aβ and α-syn pathologies are individually associated with microglia activation and
188 infiltration of peripheral myeloid cells in *in vivo* models [65-67] and in human disease[68], we aimed to
189 determine the role of co-pathologies in enhancing innate immune responses in the CNS. Co-
190 pathology and single pathology models were induced as previously stated using 12–14-week-old
191 J20 Tg or NTG littermates (Figure 1). At 3mpi, hippocampal and cortical regions were dissected
192 from co-pathology and single pathology controls for IHC analysis, mononuclear cell isolation and
193 flow cytometry (Figure 4a). Using fluorescent IHC we immunolabeled Iba1, a marker used to
194 visualize morphology of both homeostatic and activated microglia, in single pathology and co-
195 pathology brains. Compared to tau, Aβ and α-syn single pathology brains, an increased number of
196 "activated" Iba1^{+} cells were observed in the hippocampus of co-pathology mice (Figure 4b). Using
197 flow cytometry, CD11b^{+}CD45^{+} double positive myeloid cells were gated to analyze CNS resident
198 microglia (CD45^{lo}CX3CR1^{+}) and CD45^{hi} CNS macrophage populations (includes infiltrating
199 monocytes and other CNS resident macrophages) (Extended Data Figure 5a; Figure 4c). In the
200 hippocampus and cortex, the number of microglia and CD45^{hi} macrophages increased with co-
201 pathologies (Figure 4d,e). Within this CD45^{hi} population, Ly6C^{hi} infiltrating monocytes and CNS

202 resident macrophages were also increased in the hippocampus of co-pathology brains compared
203 to tau, Aβ and α-syn single pathology brains (Extended Data Figure 5d,e).
204 Given that microglia exhibit heterogeneity in health and disease based on their activation state, we
205 next profiled markers of proliferation and activation to define the specific phenotypes associated
206 with co-pathologies in the hippocampus and cortex. For this, we used CD68, a marker of
207 phagocytic activity and MHCII, a key mediator of antigen presentation to distinguish activated,
208 antigen presenting and/or phagocytic microglia. In co-pathology brains, the overall number of
209 $MHCII^{+}CD68^{+}$ microglia decreased compared to single pathologies (Extended Data Figure 5f,g).
210 Conversely, $MHCII^{-}CD68^{+}$ microglia were significantly increased in the hippocampus and cortex
211 of co-pathology mice compared to single pathology brains (Extended Data Figure 5f,g), indicating
212 a shift towards a phagocytic response. To confirm whether these phagocytic microglia are driving
213 the pro-inflammatory response due to co-pathologies, we assessed proliferation (Ki67 expression)
214 and pro-inflammatory phenotype (TLR2 expression) on $MHCII^{+}CD68^{+}$ (inflammatory
215 phagocytes) and MHCII-CD68+ (pure phagocytes) populations for functional analysis (Figure 4f).
216 $MHCII^{+}CD68^{+}$ microglia showed decreased expression of Ki67 and TLR2 (Figure 4g,h), which
217 could imply reduced antigen presentation in co-pathology brains. On the other hand, $MHCII^{-}$
218 $CD68^{+}$ microglia showed robust proliferation and $TLR2^{+}$ expression in the hippocampus and
219 cortex of co-pathology brains compared to single pathology controls (Figure 4i,j). Overall, these
220 results indicate that at 3mpi, tau, Aβ and α-syn co-pathologies synergistically promote
221 morphological and proliferative changes in microglia, translating to a more activated, phagocytic
222 state, likely to prioritize clearing the increased protein pathology load seen in co-pathology brains.
223

224 **Co-pathologies promote T cell invasion and resident memory phenotype**

225 Given the enhanced myeloid cell responses with co-pathologies[68] and the contribution of
226 peripheral $CD4^+$ and $CD8^+$ T cells to neurodegeneration *in vivo* [28,69] and in human disease[70-72], we
227 aimed to determine if T cell responses were synergistically enhanced by co-pathologies. Following
228 co-pathology induction, brains were sectioned for IHC or dissected for single-cell isolation at 3mpi
229 (Figure 5a). The presence of co-pathologies enhanced infiltration of $CD3^+$ T cells into the
230 hippocampus compared to tau, Aβ and α-syn single pathology brains (Extended Data Figure 6a,
231 Figure 5b). Utilizing mononuclear cell isolation and spectral flow cytometry, our results revealed
232 that there were significantly more $CD4^+$ and $CD8^+$ T cells in the hippocampus and cortex of co-
233 pathology brains compared tau, Aβ and α-syn single pathology mice (Figure 5c-e). This data
234 demonstrates that the presence of co-pathologies enhances the presence of both helper ($CD4^+$) and
235 cytotoxic ($CD8^+$) T cells into the brain. These data suggest that adaptive immune mechanisms
236 observed prior to neurodegeneration may be important or significantly contribute to enhanced
237 hippocampal neurodegeneration observed with co-pathology.
238
239 Tissue resident memory (Trm) T cells have been observed in human post mortem tissue in
240 neurodegenerative diseases such as AD and PD[42,73,74], where they accumulate in the brain and
241 contribute to chronic inflammation and neuronal loss[42,72]. Using cell surface markers expressed by
242 Trm T cells ($CD69^+$ and $CD103^+$) and $CD44^+$ (effector, activated T cells that are antigen
243 experienced), we examined both $CD4^+$ and $CD8^+$ Trm in the hippocampus and cortex of co-
244 pathology mice compared to single pathology mice at 3mpi. In both brain regions, co-pathologies
245 promoted a significant expansion of both $CD4^+$ and $CD8^+$ Trm ($CD62L^-CD44^+CD69^+CD103^+$)
246 relative to all single pathologies (Extended Data Figure 6b,c). $CD44^+CD4^+$ T cells and
247 $CD4^+CD69^+$ Trm (Figure 5f-h) increased by 10+ fold in co-pathology brains relative to single

248 pathology controls. $CD44^{+}CD8^{+}$ T cells and $CD8^{+}CD69^{+}CD103^{+}$ Trm were increased over 100-
249 fold in co-pathology brains compared to single pathologies (Figure 5i-k). Our findings illustrate a
250 synergistic expansion of Trm T cells, in CD4 T cells but more robust in CD8 T cells, indicating
251 that tau, Aβ and α-syn co-pathologies promote the long-term expansion and survival of antigen-
252 experienced T cells within the brain prior to overt neurodegeneration.
253

254 # Discussion

255 Tau, Aβ and α-syn as co-pathologies are pathological hallmarks of neurodegenerative
256 diseases associated with cognitive decline, however, how these protein pathologies synergize to
257 enhance neurodegeneration remains unknown. Using a novel mouse model of co-pathology
258 incorporating tau, Aβ and α-syn co-pathologies, our results demonstrate synergistic activation of
259 innate and adaptive immune responses in areas with co-expression of these accumulated proteins.
260 At 3mpi, Aβ pathology and soluble alpha-synuclein load was increased compared to the single
261 pathology controls along with a robust neuroinflammatory response, including increased
262 microglial cell number and changes in activation state, infiltration of T cells and enhanced Trm
263 signature in the cortex and hippocampus. The synergistic, not merely additive, effect of co-
264 pathologies creates a pro-inflammatory CNS environment that, in turn, enhances or accelerates
265 disease pathogenesis. Building on our previous work demonstrating that blocking
266 neuroinflammation can prevent neuronal loss in models of neurodegeneration[75,76], we propose that
267 this is largely mediated through exacerbated innate and adaptive immune responses, positioning
268 neuroinflammation as an important link between protein aggregation and neuronal loss, and a
269 prime target for combination therapy.

270 Previous studies have established that co-pathologies in mouse models can interact to
271 exacerbate disease phenotypes. DLB-AD mice (3xTg AD mice crossed with α-syn A53T mice)
272 yielded the first triple pathogenic model with worsened cognitive decline, however, there were no
273 changes in microglial reactivity[22]. Combining AD-derived tau with α-syn PFFs further enhanced
274 tau pathology and its spread relative to single pathology controls[20]. Similarly, to dissect the
275 interaction between α-syn and Aβ, 5xFAD mice were stereotaxically injected with mouse α-syn
276 PFFs to develop a 'PD-AD' mouse, that exhibited enhanced hippocampal neuronal loss, as the
277 only 'co-pathology' mouse model to assess neurodegeneration[21]. Lastly, crossing APP/PS1 mice
278 with mutant P301L tau mice has shown increased formation of Aβ plaques and tau tangles[77]. The
279 mechanism underlying this has been linked to Aβ plaques activating kinases, which leads to
280 mislocalization of tau, and subsequent hyperphosphorylation [77,78]. Results from these studies
281 demonstrate that the presence of additional pathologies promote each other's aggregation and
282 accelerate cognitive decline in mice and as such, complements the work done in human
283 postmortem studies showing co-pathology expression correlated to aging, neuroinflammation and
284 neurodegeneration[45,79]. However, likely due to the design of these models, a critical question
285 remained unanswered: whether and how tau, Aβ and α-syn synergize together as co-pathologies
286 to trigger maladaptive immune responses that directly influences enhanced neurodegeneration.
287 Within, we created a novel co-pathology mouse model to answer this question and
288 determine the effect of co-pathologies on pathological protein deposition, neuroinflammation, and
289 neurodegeneration. To model this pathological overlap seen in neurodegenerative disease, we
290 combined the AAV9-double mutant Tau (tau) and α-syn mouse PFFs (α-syn) in the same J20
291 APP^{mut} mouse (Aβ). The J20 model provides moderate, localized Aβ pathology beginning at
292 approximately 4 months old [44], while AAV-driven tau propagates from the entorhinal cortex to the

293 hippocampus and cortex to model early tau spread. As endogenous mouse tau does not aggregate
294 or form neurofibrillary tangle-like inclusions [80-82], it was important to induce the pathology in a
295 region like the entorhinal cortex, where localization allows for the propagation and subsequent
296 expression of intracellular phosphorylated tau within the hippocampus and neighboring cortices.
297 α-syn mouse PFFs induce Lewy-like inclusions with intracellular aggregation and spreading
298 throughout the limbic and cortical regions. While AAVs that overexpress α-syn in transduced
299 regions have been used to model PD[83-86], these overexpression vectors typically lack the disease-
300 like spreading pathology and only recapitulate the molecular pathology of SNCA gene
301 duplication/triplication carriers [87,88]. While this model does not fully recapitulate the spatial
302 distribution and temporal onset of pathology seen in human disease, it was designed to induce tau,
303 Aβ and α-syn pathology with their classically affected brain regions. Like most protein
304 overexpression and seeding models, it carries limitations, including the non-physiological levels
305 and a lack of gradual disease progression. While postmortem tissues offer a snapshot in time of
306 disease-driving pathology, modeling *in vivo* is needed to study interactions. Despite these caveats,
307 this model of co-pathology offers a useful tool to investigate how these pathologies synergize to
308 drive neurodegeneration and neuropathology.

309 Longitudinal and post-mortem studies from PD and AD cohorts show earlier onset of
310 cognitive decline and higher mortality rates with the presence of co-pathologies [89,90]. Based on
311 this, pure pathology is not common and may not be associated with the cognitive impairment onset
312 in these neurodegenerative diseases [45,91,92]. Here, we show that the presence of co-pathology
313 results in enhanced neuronal loss, specifically in the CA1 and CA3, regions of the hippocampus
314 compared to single pathology controls, correlating with region of enhanced pathology load in our
315 model. At the synaptic level, co-pathology mice showed reduced spine length and volume in CA1

316 pyramidal neurons, suggesting early structural remodeling that may precede or contribute to
317 neuronal loss. This suggests a link between synaptic dysfunction and functional deficits. In the
318 SNpc, however, dopaminergic neuronal loss was prominent in the co-pathology model brains
319 compared to the Aβ only brains, with no changes between tau or α-syn animals. This is likely due
320 to the localization and abundance of the co-expression of these proteins in the hippocampus,
321 suggesting a region-specific interaction of pathology burden. These results highlight the need for
322 further mechanistic studies into the additive or synergistic roles of these pathologies on
323 neurodegeneration across multiple regions.

324 Microglial activation and the infiltration of T cells have been documented in response to
325 tau, Aβ, and α-syn individually in AD and PD [93-97]. However, studies implicating the role of
326 inflammation in driving neurodegeneration in a co-pathology model are lacking. Using this novel
327 co-pathology model, we show that the co-expression of these pathologies induces robust changes
328 in microglia, and enhanced infiltration of monocytes and T cells from the periphery. Compared to
329 single pathologies, the presence of co-pathologies resulted in increased microglial cell count and
330 phenotype in the hippocampus and cortex. These changes were not limited to microglia, as we
331 observed subtle changes in the infiltrating monocyte and macrophage count in areas with co-
332 pathology burden. Our findings are consistent with recent work in human postmortem tissue that
333 compared microglia reactivity between mixed pathology (DLB+AD) brains and pure pathology
334 brains, showing higher levels of $CD68^+$, reactive microglia in the hippocampus with mixed
335 pathology [45]. In our model, $CD68^+$ microglia were synergistically enhanced by the presence of co-
336 pathology and showed heightened proliferation and TLR2 expression, while $MHCII^+$ microglia
337 decreased in number without major changes in expression of Ki67 or TLR2. Together, these
338 findings suggest that the presence of co-pathologies shifts the microglial response towards a more

339 proliferative, phagocytic phenotype, rather than a classic antigen-presenting role. Mechanistically,
340 high loads of aggregated proteins may overwhelm phagocytic pathways within microglia,
341 diverting resources toward bulk debris clearance and away from peptide processing required for
342 MHCII-mediated T cell interactions.

343 We also demonstrate enhanced T cell responses compared to single pathologies in the
344 hippocampus and cortex and synergistic expansion to Trm, marked by the expression of CD69 and
345 CD103, which are key markers for tissue retention and local immune surveillance[98,99]. Trm have
346 been shown to exacerbate disease through pro-inflammatory cytokine release and cytolytic
347 functions, which may modulate the response and activation phenotypes of local microglia [23,100].
348 The accumulation of Trm in co-pathology brain implies their prolonged, antigen-responsive
349 retention. Future studies should investigate whether co-pathologies increase the expression of
350 CXCR6 ligands (CCL19 or CCL21) by microglia or other CNS cells, as this would provide a
351 mechanistic basis for chemokine-mediated retention of Trm populations. Alternatively, there may
352 be compensatory antigen presentation by other CNS cells, like border-associated macrophages,
353 have been shown promote T cell infiltration more effectively than microglia in a neurodegenerative
354 disease model[101]. These findings suggest that chronic Trm-driven inflammation may represent a
355 converging mechanism of neurodegeneration regardless of the initiating proteinopathy. As such,
356 therapeutic strategies that focus solely on clearing a single protein species are likely insufficient.
357 Instead, combinatorial approaches that simultaneously address pathological protein accumulation
358 or modulate the immune response, particularly via Trm depletion or functional modulation of these
359 cells, may prove to be an effective strategy in altering disease course.

360 Altogether, this co-pathology model highlights a synergistic paradigm of overlapping
361 proteinopathies and an enhanced CNS-driven immune response co-existing to drive

neurodegeneration. This mirrors outcomes observed in human PD and AD patients, where both innate and adaptive responses are closely linked to disease burden. This pro-inflammatory environment may also promote microglia phagocytic activity and expansion of $CD4^+$ and $CD8^+$ Trm T cells. By demonstrating that neurodegeneration and increased protein load are co-observed with synergistic immune activation and expansion of Trm T cells, this model provides a platform to study how co-pathologies shape neuroinflammatory processes in neurodegenerative disease. These findings support the need for therapeutic strategies that address both the protein and immune landscapes of neurodegeneration.

References

1. Goedert, M. (1993). Tau protein and the neurofibrillary pathology of Alzheimer's disease. Trends Neurosci *16*, 460-465. 10.1016/0166-2236(93)90078-z.
2. Joachim, C.L., and Selkoe, D.J. (1989). Amyloid protein in Alzheimer's disease. J Gerontol *44*, B77-82. 10.1093/geronj/44.4.b77.
3. Spillantini, M.G., Schmidt, M.L., Lee, V.M., Trojanowski, J.Q., Jakes, R., and Goedert, M. (1997). Alpha-synuclein in Lewy bodies. Nature *388*, 839-840. 10.1038/42166.
4. Irwin, D.J., Grossman, M., Weintraub, D., Hurtig, H.I., Duda, J.E., Xie, S.X., Lee, E.B., Van Deerlin, V.M., Lopez, O.L., Kofler, J.K., et al. (2017). Neuropathological and genetic correlates of survival and dementia onset in synucleinopathies: a retrospective analysis. Lancet Neurol *16*, 55-65. 10.1016/s1474-4422(16)30291-5.
5. Irwin, D.J., Xie, S.X., Coughlin, D., Nevler, N., Akhtar, R.S., McMillan, C.T., Lee, E.B., Wolk, D.A., Weintraub, D., Chen-Plotkin, A., et al. (2018). CSF tau and β-amyloid predict cerebral synucleinopathy in autopsied Lewy body disorders. Neurology *90*, e1038-e1046. 10.1212/wnl.0000000000005166.
6. Jellinger, K.A. (2002). Alzheimer disease and cerebrovascular pathology: an update. J Neural Transm (Vienna) *109*, 813-836. 10.1007/s007020200068.
7. Jellinger, K.A. (2003). Alpha-synuclein pathology in Parkinson's and Alzheimer's disease brain: incidence and topographic distribution--a pilot study. Acta Neuropathol *106*, 191-201. 10.1007/s00401-003-0725-y.
8. Jellinger, K.A. (2020). Neuropathological assessment of the Alzheimer spectrum. J Neural Transm (Vienna) *127*, 1229-1256. 10.1007/s00702-020-02232-9.
9. Kotzbauer, P.T., Cairns, N.J., Campbell, M.C., Willis, A.W., Racette, B.A., Tabbal, S.D., and Perlmutter, J.S. (2012). Pathologic accumulation of α-synuclein and Aβ in Parkinson

396 disease patients with dementia. Arch Neurol *69*, 1326-1331.
397 10.1001/archneurol.2012.1608.
398 10. Robinson, J.L., Lee, E.B., Xie, S.X., Rennert, L., Suh, E., Bredenberg, C., Caswell, C., Van
399 Deerlin, V.M., Yan, N., Yousef, A., et al. (2018). Neurodegenerative disease concomitant
400 proteinopathies are prevalent, age-related and APOE4-associated. Brain *141*, 2181-2193.
401 10.1093/brain/awy146.
402 11. Spires-Jones, T.L., Attems, J., and Thal, D.R. (2017). Interactions of pathological proteins
403 in neurodegenerative diseases. Acta Neuropathol *134*, 187-205. 10.1007/s00401-017-
404 1709-7.
405 12. Compta, Y., Parkkinen, L., Kempster, P., Selikhova, M., Lashley, T., Holton, J.L., Lees,
406 A.J., and Revesz, T. (2014). The significance of α-synuclein, amyloid-β and tau pathologies
407 in Parkinson's disease progression and related dementia. Neurodegener Dis *13*, 154-156.
408 10.1159/000354670.
409 13. Twohig, D., and Nielsen, H.M. (2019). α-synuclein in the pathophysiology of Alzheimer's
410 disease. Mol Neurodegener *14*, 23. 10.1186/s13024-019-0320-x.
411 14. van der Gaag, B.L., Deshayes, N.A.C., Breve, J.J.P., Bol, J., Jonker, A.J., Hoozemans,
412 J.J.M., Courade, J.P., and van de Berg, W.D.J. (2024). Distinct tau and alpha-synuclein
413 molecular signatures in Alzheimer's disease with and without Lewy bodies and Parkinson's
414 disease with dementia. Acta Neuropathol *147*, 14. 10.1007/s00401-023-02657-y.
415 15. Franzmeier, N., Roemer-Cassiano, S.N., Bernhardt, A.M., Dehsarvi, A., Dewenter, A.,
416 Steward, A., Biel, D., Frontzkowski, L., Zhu, Z., Gnörich, J., et al. (2025). Alpha synuclein
417 co-pathology is associated with accelerated amyloid-driven tau accumulation in
418 Alzheimer's disease. Molecular Neurodegeneration *20*, 31. 10.1186/s13024-025-00822-3.
419 16. Coughlin, D., Xie, S.X., Liang, M., Williams, A., Peterson, C., Weintraub, D., McMillan,
420 C.T., Wolk, D.A., Akhtar, R.S., Hurtig, H.I., et al. (2019). Cognitive and Pathological
421 Influences of Tau Pathology in Lewy Body Disorders. Ann Neurol *85*, 259-271.
422 10.1002/ana.25392.
423 17. Kraybill, M.L., Larson, E.B., Tsuang, D.W., Teri, L., McCormick, W.C., Bowen, J.D.,
424 Kukull, W.A., Leverenz, J.B., and Cherrier, M.M. (2005). Cognitive differences in
425 dementia patients with autopsy-verified AD, Lewy body pathology, or both. Neurology *64*,
426 2069-2073. 10.1212/01.WNL.0000165987.89198.65.
427 18. Mak, E., Reid, R.I., Przybelski, S.A., Lesnick, T.G., Schwarz, C.G., Senjem, M.L.,
428 Raghavan, S., Vemuri, P., Jack, C.R., Jr., Min, H.K., et al. (2024). Influences of amyloid-β
429 and tau on white matter neurite alterations in dementia with Lewy bodies. NPJ Parkinsons
430 Dis *10*, 76. 10.1038/s41531-024-00684-4.
431 19. Malek-Ahmadi, M., Beach, T.G., Zamrini, E., Adler, C.H., Sabbagh, M.N., Shill, H.A.,
432 Jacobson, S.A., Belden, C.M., Caselli, R.J., Woodruff, B.K., et al. (2019). Faster cognitive
433 decline in dementia due to Alzheimer disease with clinically undiagnosed Lewy body
434 disease. PLoS One *14*, e0217566. 10.1371/journal.pone.0217566.
435 20. Bassil, F., Brown, H.J., Pattabhiraman, S., Iwasyk, J.E., Maghames, C.M., Meymand, E.S.,
436 Cox, T.O., Riddle, D.M., Zhang, B., Trojanowski, J.Q., and Lee, V.M. (2020). Amyloid-
437 Beta (Aβ) Plaques Promote Seeding and Spreading of Alpha-Synuclein and Tau in a Mouse
438 Model of Lewy Body Disorders with Aβ Pathology. Neuron *105*, 260-275.e266.
439 10.1016/j.neuron.2019.10.010.

21. Bassil, F., Meymand, E.S., Brown, H.J., Xu, H., Cox, T.O., Pattabhiraman, S., Maghames, C.M., Wu, Q., Zhang, B., Trojanowski, J.Q., and Lee, V.M. (2021). α-Synuclein modulates tau spreading in mouse brains. J Exp Med *218*. 10.1084/jem.20192193.
22. Clinton, L.K., Blurton-Jones, M., Myczek, K., Trojanowski, J.Q., and LaFerla, F.M. (2010). Synergistic Interactions between Abeta, tau, and alpha-synuclein: acceleration of neuropathology and cognitive decline. J Neurosci *30*, 7281-7289. 10.1523/JNEUROSCI.0490-10.2010.
23. Gate, D., Saligrama, N., Leventhal, O., Yang, A.C., Unger, M.S., Middeldorp, J., Chen, K., Lehallier, B., Channappa, D., De Los Santos, M.B., et al. (2020). Clonally expanded CD8 T cells patrol the cerebrospinal fluid in Alzheimer's disease. Nature *577*, 399-404. 10.1038/s41586-019-1895-7.
24. Itagaki, S., McGeer, P.L., and Akiyama, H. (1988). Presence of T-cytotoxic suppressor and leucocyte common antigen positive cells in Alzheimer's disease brain tissue. Neurosci Lett *91*, 259-264. 10.1016/0304-3940(88)90690-8.
25. Merlini, M., Kirabali, T., Kulic, L., Nitsch, R.M., and Ferretti, M.T. (2018). Extravascular CD3+ T Cells in Brains of Alzheimer Disease Patients Correlate with Tau but Not with Amyloid Pathology: An Immunohistochemical Study. Neurodegener Dis *18*, 49-56. 10.1159/000486200.
26. Rogers, J., Luber-Narod, J., Styren, S.D., and Civin, W.H. (1988). Expression of immune system-associated antigens by cells of the human central nervous system: relationship to the pathology of Alzheimer's disease. Neurobiol Aging *9*, 339-349. 10.1016/s0197-4580(88)80079-4.
27. Togo, T., Akiyama, H., Iseki, E., Kondo, H., Ikeda, K., Kato, M., Oda, T., Tsuchiya, K., and Kosaka, K. (2002). Occurrence of T cells in the brain of Alzheimer's disease and other neurological diseases. J Neuroimmunol *124*, 83-92. 10.1016/s0165-5728(01)00496-9.
28. Brochard, V., Combadiere, B., Prigent, A., Laouar, Y., Perrin, A., Beray-Berthat, V., Bonduelle, O., Alvarez-Fischer, D., Callebert, J., Launay, J.M., et al. (2009). Infiltration of CD4+ lymphocytes into the brain contributes to neurodegeneration in a mouse model of Parkinson disease. J Clin Invest *119*, 182-192. 10.1172/JCI36470.
29. Sulzer, D., Alcalay, R.N., Garretti, F., Cote, L., Kanter, E., Agin-Liebes, J., Liong, C., McMurtrey, C., Hildebrand, W.H., Mao, X., et al. (2017). T cells from patients with Parkinson's disease recognize α-synuclein peptides. Nature *546*, 656-661. 10.1038/nature22815.
30. Yan, Z., Yang, W., Wei, H., Dean, M.N., Standaert, D.G., Cutter, G.R., Benveniste, E.N., and Qin, H. (2021). Dysregulation of the Adaptive Immune System in Patients With Early-Stage Parkinson Disease. Neurol Neuroimmunol Neuroinflamm *8*. 10.1212/NXI.0000000000001036.
31. Ries, M., and Sastre, M. (2016). Mechanisms of Aβ Clearance and Degradation by Glial Cells. Front Aging Neurosci *8*, 160. 10.3389/fnagi.2016.00160.
32. Zhao, Y., Wu, X., Li, X., Jiang, L.L., Gui, X., Liu, Y., Sun, Y., Zhu, B., Piña-Crespo, J.C., Zhang, M., et al. (2018). TREM2 Is a Receptor for β-Amyloid that Mediates Microglial Function. Neuron *97*, 1023-1031.e1027. 10.1016/j.neuron.2018.01.031.
33. Keren-Shaul, H., Spinrad, A., Weiner, A., Matcovitch-Natan, O., Dvir-Szternfeld, R., Ulland, T.K., David, E., Baruch, K., Lara-Astaiso, D., Toth, B., et al. (2017). A Unique Microglia Type Associated with Restricting Development of Alzheimer's Disease. Cell *169*, 1276-1290.e1217. 10.1016/j.cell.2017.05.018.

34. Pampuscenko, K., Morkuniene, R., Krasauskas, L., Smirnovas, V., Brown, G.C., and Borutaite, V. (2023). Extracellular tau stimulates phagocytosis of living neurons by activated microglia via Toll-like 4 receptor-NLRP3 inflammasome-caspase-1 signalling axis. Sci Rep *13*, 10813. 10.1038/s41598-023-37887-3.
35. Chen, X., Firulyova, M., Manis, M., Herz, J., Smirnov, I., Aladyeva, E., Wang, C., Bao, X., Finn, M.B., Hu, H., et al. (2023). Microglia-mediated T cell infiltration drives neurodegeneration in tauopathy. Nature *615*, 668-677. 10.1038/s41586-023-05788-0.
36. Karpenko, M.N., Vasilishina, A.A., Gromova, E.A., Muruzheva, Z.M., Miliukhina, I.V., and Bernadotte, A. (2018). Interleukin-1β, interleukin-1 receptor antagonist, interleukin-6, interleukin-10, and tumor necrosis factor-α levels in CSF and serum in relation to the clinical diversity of Parkinson's disease. Cell Immunol *327*, 77-82. 10.1016/j.cellimm.2018.02.011.
37. Ma, M., Paryani, F., Jakubiak, K., Xia, S., Antoku, S., Kannan, A., Lee, J., Madden, N., Senthil Kumar, S., Li, J., et al. (2025). The spatial landscape of glial pathology and T cell response in Parkinson's disease substantia nigra. Nature Communications *16*, 7146. 10.1038/s41467-025-62478-3.
38. Sulzer, D., Alcalay, R.N., Garretti, F., Cote, L., Kanter, E., Agin-Liebes, J., Liong, C., McMurtrey, C., Hildebrand, W.H., Mao, X., et al. (2017). T cells from patients with Parkinson's disease recognize alpha-synuclein peptides. Nature *546*, 656-661. 10.1038/nature22815.
39. Altendorfer, B., Unger, M.S., Poupardin, R., Hoog, A., Asslaber, D., Gratz, I.K., Mrowetz, H., Benedetti, A., de Sousa, D.M.B., Greil, R., et al. (2022). Transcriptomic Profiling Identifies CD8(+) T Cells in the Brain of Aged and Alzheimer's Disease Transgenic Mice as Tissue-Resident Memory T Cells. J Immunol *209*, 1272-1285. 10.4049/jimmunol.2100737.
40. Galiano-Landeira, J., Torra, A., Vila, M., and Bové, J. (2020). CD8 T cell nigral infiltration precedes synucleinopathy in early stages of Parkinson's disease. Brain *143*, 3717-3733. 10.1093/brain/awaa269.
41. Hefendehl, J.K., Neher, J.J., Sühs, R.B., Kohsaka, S., Skodras, A., and Jucker, M. (2014). Homeostatic and injury-induced microglia behavior in the aging brain. Aging Cell *13*, 60-69. 10.1111/acel.12149.
42. Kimura, K., Nishigori, R., Hamatani, M., Sawamura, M., Ashida, S., Fujii, C., Takata, M., Lin, Y., Sato, W., Okamoto, T., et al. (2024). Resident Memory-like CD8(+) T Cells Are Involved in Chronic Inflammatory and Neurodegenerative Diseases in the CNS. Neurol Neuroimmunol Neuroinflamm *11*. 10.1212/nxi.0000000000200172.
43. Wang, P., Yao, L., Luo, M., Zhou, W., Jin, X., Xu, Z., Yan, S., Li, Y., Xu, C., Cheng, R., et al. (2021). Single-cell transcriptome and TCR profiling reveal activated and expanded T cell populations in Parkinson's disease. Cell Discov *7*, 52. 10.1038/s41421-021-00280-3.
44. Mucke, L., Masliah, E., Yu, G.Q., Mallory, M., Rockenstein, E.M., Tatsuno, G., Hu, K., Kholodenko, D., Johnson-Wood, K., and McConlogue, L. (2000). High-level neuronal expression of abeta 1-42 in wild-type human amyloid protein precursor transgenic mice: synaptotoxicity without plaque formation. J Neurosci *20*, 4050-4058.
45. Wetering, J.V., Geut, H., Bol, J.J., Galis, Y., Timmermans, E., Twisk, J.W.R., Hepp, D.H., Morella, M.L., Pihlstrom, L., Lemstra, A.W., et al. (2024). Neuroinflammation is associated with Alzheimer's disease co-pathology in dementia with Lewy bodies. Acta Neuropathol Commun *12*, 73. 10.1186/s40478-024-01786-z.

46. Colom-Cadena, M., Gelpi, E., Charif, S., Belbin, O., Blesa, R., Martí, M.J., Clarimón, J., and Lleó, A. (2013). Confluence of α-synuclein, tau, and β-amyloid pathologies in dementia with Lewy bodies. J Neuropathol Exp Neurol *72*, 1203-1212. 10.1097/nen.0000000000000018.
47. Ferman, T.J., Aoki, N., Crook, J.E., Murray, M.E., Graff-Radford, N.R., van Gerpen, J.A., Uitti, R.J., Wszolek, Z.K., Graff-Radford, J., Pedraza, O., et al. (2018). The limbic and neocortical contribution of α-synuclein, tau, and amyloid β to disease duration in dementia with Lewy bodies. Alzheimers Dement *14*, 330-339. 10.1016/j.jalz.2017.09.014.
48. Kouli, A., Camacho, M., Allinson, K., and Williams-Gray, C.H. (2020). Neuroinflammation and protein pathology in Parkinson's disease dementia. Acta Neuropathol Commun *8*, 211. 10.1186/s40478-020-01083-5.
49. Irwin, D.J., Lee, V.M., and Trojanowski, J.Q. (2013). Parkinson's disease dementia: convergence of alpha-synuclein, tau and amyloid-beta pathologies. Nat Rev Neurosci *14*, 626-636. 10.1038/nrn3549.
50. Sengupta, U., and Kayed, R. (2022). Amyloid β, Tau, and α-Synuclein aggregates in the pathogenesis, prognosis, and therapeutics for neurodegenerative diseases. Prog Neurobiol *214*, 102270. 10.1016/j.pneurobio.2022.102270.
51. Braak, H., Del Tredici, K., Rüb, U., de Vos, R.A., Jansen Steur, E.N., and Braak, E. (2003). Staging of brain pathology related to sporadic Parkinson's disease. Neurobiol Aging *24*, 197-211. 10.1016/s0197-4580(02)00065-9.
52. DeKosky, S.T., and Scheff, S.W. (1990). Synapse loss in frontal cortex biopsies in Alzheimer's disease: correlation with cognitive severity. Ann Neurol *27*, 457-464. 10.1002/ana.410270502.
53. Greffard, S., Verny, M., Bonnet, A.M., Beinis, J.Y., Gallinari, C., Meaume, S., Piette, F., Hauw, J.J., and Duyckaerts, C. (2006). Motor score of the Unified Parkinson Disease Rating Scale as a good predictor of Lewy body-associated neuronal loss in the substantia nigra. Arch Neurol *63*, 584-588. 10.1001/archneur.63.4.584.
54. Selkoe, D.J. (2002). Alzheimer's disease is a synaptic failure. Science *298*, 789-791. 10.1126/science.1074069.
55. Busche, M.A., Chen, X., Henning, H.A., Reichwald, J., Staufenbiel, M., Sakmann, B., and Konnerth, A. (2012). Critical role of soluble amyloid-β for early hippocampal hyperactivity in a mouse model of Alzheimer’s disease. Proceedings of the National Academy of Sciences *109*, 8740-8745. doi:10.1073/pnas.1206171109.
56. Shabir, O., Sharp, P., Rebollar, M.A., Boorman, L., Howarth, C., Wharton, S.B., Francis, S.E., and Berwick, J. (2020). Enhanced Cerebral Blood Volume under Normobaric Hyperoxia in the J20-hAPP Mouse Model of Alzheimer’s Disease. Scientific Reports *10*, 7518. 10.1038/s41598-020-64334-4.
57. Bourne, J.N., and Harris, K.M. (2008). Balancing structure and function at hippocampal dendritic spines. Annu Rev Neurosci *31*, 47-67. 10.1146/annurev.neuro.31.060407.125646.
58. Knobloch, M., and Mansuy, I.M. (2008). Dendritic spine loss and synaptic alterations in Alzheimer's disease. Mol Neurobiol *37*, 73-82. 10.1007/s12035-008-8018-z.
59. Spires-Jones, T.L., and Hyman, B.T. (2014). The intersection of amyloid beta and tau at synapses in Alzheimer's disease. Neuron *82*, 756-771. 10.1016/j.neuron.2014.05.004.
60. Double, K.L. (2012). Neuronal vulnerability in Parkinson's disease. Parkinsonism Relat Disord *18 Suppl 1*, S52-54. 10.1016/s1353-8020(11)70018-9.

578 61. Giguère, N., Burke Nanni, S., and Trudeau, L.E. (2018). On Cell Loss and Selective
579 Vulnerability of Neuronal Populations in Parkinson's Disease. Front Neurol *9*, 455.
580 10.3389/fneur.2018.00455.
581 62. Mrdjen, D., Fox, E.J., Bukhari, S.A., Montine, K.S., Bendall, S.C., and Montine, T.J.
582 (2019). The basis of cellular and regional vulnerability in Alzheimer's disease. Acta
583 Neuropathol *138*, 729-749. 10.1007/s00401-019-02054-4.
584 63. Olajide, O.J., Suvanto, M.E., and Chapman, C.A. (2021). Molecular mechanisms of
585 neurodegeneration in the entorhinal cortex that underlie its selective vulnerability during
586 the pathogenesis of Alzheimer's disease. Biol Open *10*. 10.1242/bio.056796.
587 64. Buchman, A.S., and Bennett, D.A. (2011). Loss of motor function in preclinical
588 Alzheimer's disease. Expert Rev Neurother *11*, 665-676. 10.1586/ern.11.57.
589 65. Harms, A.S., Thome, A.D., Yan, Z., Schonhoff, A.M., Williams, G.P., Li, X., Liu, Y., Qin,
590 H., Benveniste, E.N., and Standaert, D.G. (2018). Peripheral monocyte entry is required
591 for alpha-Synuclein induced inflammation and Neurodegeneration in a model of Parkinson
592 disease. Exp Neurol *300*, 179-187. 10.1016/j.expneurol.2017.11.010.
593 66. Heneka, M.T., Kummer, M.P., Stutz, A., Delekate, A., Schwartz, S., Vieira-Saecker, A.,
594 Griep, A., Axt, D., Remus, A., Tzeng, T.C., et al. (2013). NLRP3 is activated in Alzheimer's
595 disease and contributes to pathology in APP/PS1 mice. Nature *493*, 674-678.
596 10.1038/nature11729.
597 67. Maphis, N., Xu, G., Kokiko-Cochran, O.N., Jiang, S., Cardona, A., Ransohoff, R.M.,
598 Lamb, B.T., and Bhaskar, K. (2015). Reactive microglia drive tau pathology and contribute
599 to the spreading of pathological tau in the brain. Brain *138*, 1738-1755.
600 10.1093/brain/awv081.
601 68. Wetering, J.v., Geut, H., Bol, J.J., Galis, Y., Timmermans, E., Twisk, J.W.R., Hepp, D.H.,
602 Morella, M.L., Pihlstrom, L., Lemstra, A.W., et al. (2024). Neuroinflammation is
603 associated with Alzheimer's disease co-pathology in dementia with Lewy bodies. Acta
604 Neuropathologica Communications *12*, 73. 10.1186/s40478-024-01786-z.
605 69. Ferretti, M.T., Merlini, M., Späni, C., Gericke, C., Schweizer, N., Enzmann, G.,
606 Engelhardt, B., Kulic, L., Suter, T., and Nitsch, R.M. (2016). T-cell brain infiltration and
607 immature antigen-presenting cells in transgenic models of Alzheimer's disease-like
608 cerebral amyloidosis. Brain Behav Immun *54*, 211-225. 10.1016/j.bbi.2016.02.009.
609 70. Gate, D., Tapp, E., Leventhal, O., Shahid, M., Nonninger, T.J., Yang, A.C., Strempfl, K.,
610 Unger, M.S., Fehlmann, T., Oh, H., et al. (2021). CD4(+) T cells contribute to
611 neurodegeneration in Lewy body dementia. Science *374*, 868-874.
612 10.1126/science.abf7266.
613 71. Haage, V., and De Jager, P.L. (2022). Neuroimmune contributions to Alzheimer's disease:
614 a focus on human data. Mol Psychiatry *27*, 3164-3181. 10.1038/s41380-022-01637-0.
615 72. Yamakawa, M., and Rexach, J.E. (2024). Cell States and Interactions of CD8 T Cells and
616 Disease-Enriched Microglia in Human Brains with Alzheimer's Disease. Biomedicines *12*.
617 10.3390/biomedicines12020308.
618 73. Gate, D., Saligrama, N., Leventhal, O., Yang, A.C., Unger, M.S., Middeldorp, J., Chen, K.,
619 Lehallier, B., Channappa, D., De Los Santos, M.B., et al. (2020). Clonally expanded CD8
620 T cells patrol the cerebrospinal fluid in Alzheimer's disease. Nature *577*, 399-404.
621 10.1038/s41586-019-1895-7.
622 74. Su, W., Saravia, J., Risch, I., Rankin, S., Guy, C., Chapman, N.M., Shi, H., Sun, Y., Kc, A.,
623 Li, W., et al. (2023). CXCR6 orchestrates brain CD8(+) T cell residency and limits mouse

624 Alzheimer's disease pathology. Nat Immunol *24*, 1735-1747. 10.1038/s41590-023-01604-
625 z.
626 75. Corbin-Stein, N.J., Childers, G.M., Webster, J.M., Zane, A., Yang, Y.-T., Mudium, N.,
627 Gupta, R., Manfredsson, F.P., Kordower, J.H., and Harms, A.S. (2024). IFNγ drives
628 neuroinflammation, demyelination, and neurodegeneration in a mouse model of multiple
629 system atrophy. Acta Neuropathologica Communications *12*, 11. 10.1186/s40478-023-
630 01710-x.
631 76. Williams, G.P., Schonhoff, A.M., Jurkuvenaite, A., Thome, A.D., Standaert, D.G., and
632 Harms, A.S. (2018). Targeting of the class II transactivator attenuates inflammation and
633 neurodegeneration in an alpha-synuclein model of Parkinson's disease. J
634 Neuroinflammation *15*, 244. 10.1186/s12974-018-1286-2.
635 77. Lewis, J., Dickson, D.W., Lin, W.L., Chisholm, L., Corral, A., Jones, G., Yen, S.H., Sahara,
636 N., Skipper, L., Yager, D., et al. (2001). Enhanced neurofibrillary degeneration in
637 transgenic mice expressing mutant tau and APP. Science *293*, 1487-1491.
638 10.1126/science.1058189.
639 78. Shipton, O.A., Leitz, J.R., Dworzak, J., Acton, C.E., Tunbridge, E.M., Denk, F., Dawson,
640 H.N., Vitek, M.P., Wade-Martins, R., Paulsen, O., and Vargas-Caballero, M. (2011). Tau
641 protein is required for amyloid {beta}-induced impairment of hippocampal long-term
642 potentiation. J Neurosci *31*, 1688-1692. 10.1523/jneurosci.2610-10.2011.
643 79. Schneider, J.A., Arvanitakis, Z., Bang, W., and Bennett, D.A. (2007). Mixed brain
644 pathologies account for most dementia cases in community-dwelling older persons.
645 Neurology *69*, 2197-2204. 10.1212/01.wnl.0000271090.28148.24.
646 80. Andorfer, C., Kress, Y., Espinoza, M., de Silva, R., Tucker, K.L., Barde, Y.A., Duff, K.,
647 and Davies, P. (2003). Hyperphosphorylation and aggregation of tau in mice expressing
648 normal human tau isoforms. J Neurochem *86*, 582-590. 10.1046/j.1471-
649 4159.2003.01879.x.
650 81. Duff, K., Eckman, C., Zehr, C., Yu, X., Prada, C.M., Perez-tur, J., Hutton, M., Buee, L.,
651 Harigaya, Y., Yager, D., et al. (1996). Increased amyloid-beta42(43) in brains of mice
652 expressing mutant presenilin 1. Nature *383*, 710-713. 10.1038/383710a0.
653 82. Lewis, J., McGowan, E., Rockwood, J., Melrose, H., Nacharaju, P., Van Slegtenhorst, M.,
654 Gwinn-Hardy, K., Paul Murphy, M., Baker, M., Yu, X., et al. (2000). Neurofibrillary
655 tangles, amyotrophy and progressive motor disturbance in mice expressing mutant (P301L)
656 tau protein. Nat Genet *25*, 402-405. 10.1038/78078.
657 83. Decressac, M., Mattsson, B., Lundblad, M., Weikop, P., and Björklund, A. (2012).
658 Progressive neurodegenerative and behavioural changes induced by AAV-mediated
659 overexpression of α-synuclein in midbrain dopamine neurons. Neurobiol Dis *45*, 939-953.
660 10.1016/j.nbd.2011.12.013.
661 84. Elabi, O., Gaceb, A., Carlsson, R., Padel, T., Soylu-Kucharz, R., Cortijo, I., Li, W., Li, J.Y.,
662 and Paul, G. (2021). Human α-synuclein overexpression in a mouse model of Parkinson's
663 disease leads to vascular pathology, blood brain barrier leakage and pericyte activation. Sci
664 Rep *11*, 1120. 10.1038/s41598-020-80889-8.
665 85. Karikari, A.A., McFleder, R.L., Ribechini, E., Blum, R., Bruttel, V., Knorr, S., Gehmeyr,
666 M., Volkmann, J., Brotchie, J.M., Ahsan, F., et al. (2022). Neurodegeneration by α-
667 synuclein-specific T cells in AAV-A53T-α-synuclein Parkinson's disease mice. Brain
668 Behav Immun *101*, 194-210. 10.1016/j.bbi.2022.01.007.

86. Schonhoff, A.M., Figge, D.A., Williams, G.P., Jurkuvenaite, A., Gallups, N.J., Childers, G.M., Webster, J.M., Standaert, D.G., Goldman, J.E., and Harms, A.S. (2023). Border-associated macrophages mediate the neuroinflammatory response in an alpha-synuclein model of Parkinson disease. Nat Commun *14*, 3754. 10.1038/s41467-023-39060-w.
87. Gómez-Benito, M., Granado, N., García-Sanz, P., Michel, A., Dumoulin, M., and Moratalla, R. (2020). Modeling Parkinson's Disease With the Alpha-Synuclein Protein. Front Pharmacol *11*, 356. 10.3389/fphar.2020.00356.
88. Pinto-Costa, R., Harbachova, E., La Vitola, P., and Di Monte, D.A. (2023). Overexpression-Induced α-Synuclein Brain Spreading. Neurotherapeutics *20*, 83-96. 10.1007/s13311-022-01332-6.
89. Irwin, D.J., Lee, V.M., and Trojanowski, J.Q. (2013). Parkinson's disease dementia: convergence of α-synuclein, tau and amyloid-β pathologies. Nat Rev Neurosci *14*, 626-636. 10.1038/nrn3549.
90. Lim, A., Tsuang, D., Kukull, W., Nochlin, D., Leverenz, J., McCormick, W., Bowen, J., Teri, L., Thompson, J., Peskind, E.R., et al. (1999). Clinico-neuropathological correlation of Alzheimer's disease in a community-based case series. J Am Geriatr Soc *47*, 564-569. 10.1111/j.1532-5415.1999.tb02571.x.
91. Lashley, T., Holton, J.L., Gray, E., Kirkham, K., O'Sullivan, S.S., Hilbig, A., Wood, N.W., Lees, A.J., and Revesz, T. (2008). Cortical alpha-synuclein load is associated with amyloid-beta plaque burden in a subset of Parkinson's disease patients. Acta Neuropathol *115*, 417-425. 10.1007/s00401-007-0336-0.
92. Nelson, P.T., Braak, H., and Markesbery, W.R. (2009). Neuropathology and cognitive impairment in Alzheimer disease: a complex but coherent relationship. J Neuropathol Exp Neurol *68*, 1-14. 10.1097/NEN.0b013e3181919a48.
93. Chen, Y., and Yu, Y. (2023). Tau and neuroinflammation in Alzheimer's disease: interplay mechanisms and clinical translation. J Neuroinflammation *20*, 165. 10.1186/s12974-023-02853-3.
94. Hansen, D.V., Hanson, J.E., and Sheng, M. (2018). Microglia in Alzheimer's disease. J Cell Biol *217*, 459-472. 10.1083/jcb.201709069.
95. Heneka, M.T., Carson, M.J., El Khoury, J., Landreth, G.E., Brosseron, F., Feinstein, D.L., Jacobs, A.H., Wyss-Coray, T., Vitorica, J., Ransohoff, R.M., et al. (2015). Neuroinflammation in Alzheimer's disease. Lancet Neurol *14*, 388-405. 10.1016/s1474-4422(15)70016-5.
96. Imamura, K., Hishikawa, N., Sawada, M., Nagatsu, T., Yoshida, M., and Hashizume, Y. (2003). Distribution of major histocompatibility complex class II-positive microglia and cytokine profile of Parkinson's disease brains. Acta Neuropathol *106*, 518-526. 10.1007/s00401-003-0766-2.
97. Zeng, J., Liao, Z., Yang, H., Wang, Q., Wu, Z., Hua, F., and Zhou, Z. (2024). T cell infiltration mediates neurodegeneration and cognitive decline in Alzheimer's disease. Neurobiol Dis *193*, 106461. 10.1016/j.nbd.2024.106461.
98. Smolders, J., Heutinck, K.M., Fransen, N.L., Remmerswaal, E.B.M., Hombrink, P., Ten Berge, I.J.M., van Lier, R.A.W., Huitinga, I., and Hamann, J. (2018). Tissue-resident memory T cells populate the human brain. Nat Commun *9*, 4593. 10.1038/s41467-018-07053-9.

99. Wakim, L.M., Woodward-Davis, A., and Bevan, M.J. (2010). Memory T cells persisting within the brain after local infection show functional adaptations to their tissue of residence. Proc Natl Acad Sci U S A *107*, 17872-17879. 10.1073/pnas.1010201107.
100. Smolders, J., Remmerswaal, E.B., Schuurman, K.G., Melief, J., van Eden, C.G., van Lier, R.A., Huitinga, I., and Hamann, J. (2013). Characteristics of differentiated CD8(+) and CD4 (+) T cells present in the human brain. Acta Neuropathol *126*, 525-535. 10.1007/s00401-013-1155-0.
101. Schonhoff, A.M., Figge, D.A., Williams, G.P., Jurkuvenaite, A., Gallups, N.J., Childers, G.M., Webster, J.M., Standaert, D.G., Goldman, J.E., and Harms, A.S. (2023). Border-associated macrophages mediate the neuroinflammatory response in an alpha-synuclein model of Parkinson disease. Nature Communications *14*, 3754. 10.1038/s41467-023-39060-w.
102. Luk, K.C., Song, C., O'Brien, P., Stieber, A., Branch, J.R., Brunden, K.R., Trojanowski, J.Q., and Lee, V.M. (2009). Exogenous alpha-synuclein fibrils seed the formation of Lewy body-like intracellular inclusions in cultured cells. Proc Natl Acad Sci U S A *106*, 20051-20056. 10.1073/pnas.0908005106.
103. Volpicelli-Daley, L.A., Luk, K.C., and Lee, V.M. (2014). Addition of exogenous α-synuclein preformed fibrils to primary neuronal cultures to seed recruitment of endogenous α-synuclein to Lewy body and Lewy neurite-like aggregates. Nat Protoc *9*, 2135-2146. 10.1038/nprot.2014.143.
104. Gray, S.J., Foti, S.B., Schwartz, J.W., Bachaboina, L., Taylor-Blake, B., Coleman, J., Ehlers, M.D., Zylka, M.J., McCown, T.J., and Samulski, R.J. (2011). Optimizing promoters for recombinant adeno-associated virus-mediated gene expression in the peripheral and central nervous system using self-complementary vectors. Hum Gene Ther *22*, 1143-1153. 10.1089/hum.2010.245.
105. Sandoval, I.M., Kuhn, N.M., and Manfredsson, F.P. (2019). Multimodal Production of Adeno-Associated Virus. Methods Mol Biol *1937*, 101-124. 10.1007/978-1-4939-9065-8_6.
106. Greathouse, K.M., Henderson, B.W., Gentry, E.G., and Herskowitz, J.H. (2019). Fasudil or genetic depletion of ROCK1 or ROCK2 induces anxiety-like behaviors. Behav Brain Res *373*, 112083. 10.1016/j.bbr.2019.112083.
107. Henderson, B.W., Greathouse, K.M., Ramdas, R., Walker, C.K., Rao, T.C., Bach, S.V., Curtis, K.A., Day, J.J., Mattheyses, A.L., and Herskowitz, J.H. (2019). Pharmacologic inhibition of LIMK1 provides dendritic spine resilience against β-amyloid. Science Signaling *12*, eaaw9318. doi:10.1126/scisignal.aaw9318.
108. Greathouse, K.M., Boros, B.D., Deslauriers, J.F., Henderson, B.W., Curtis, K.A., Gentry, E.G., and Herskowitz, J.H. (2018). Distinct and complementary functions of rho kinase isoforms ROCK1 and ROCK2 in prefrontal cortex structural plasticity. Brain Struct Funct *223*, 4227-4241. 10.1007/s00429-018-1748-4.

Figures

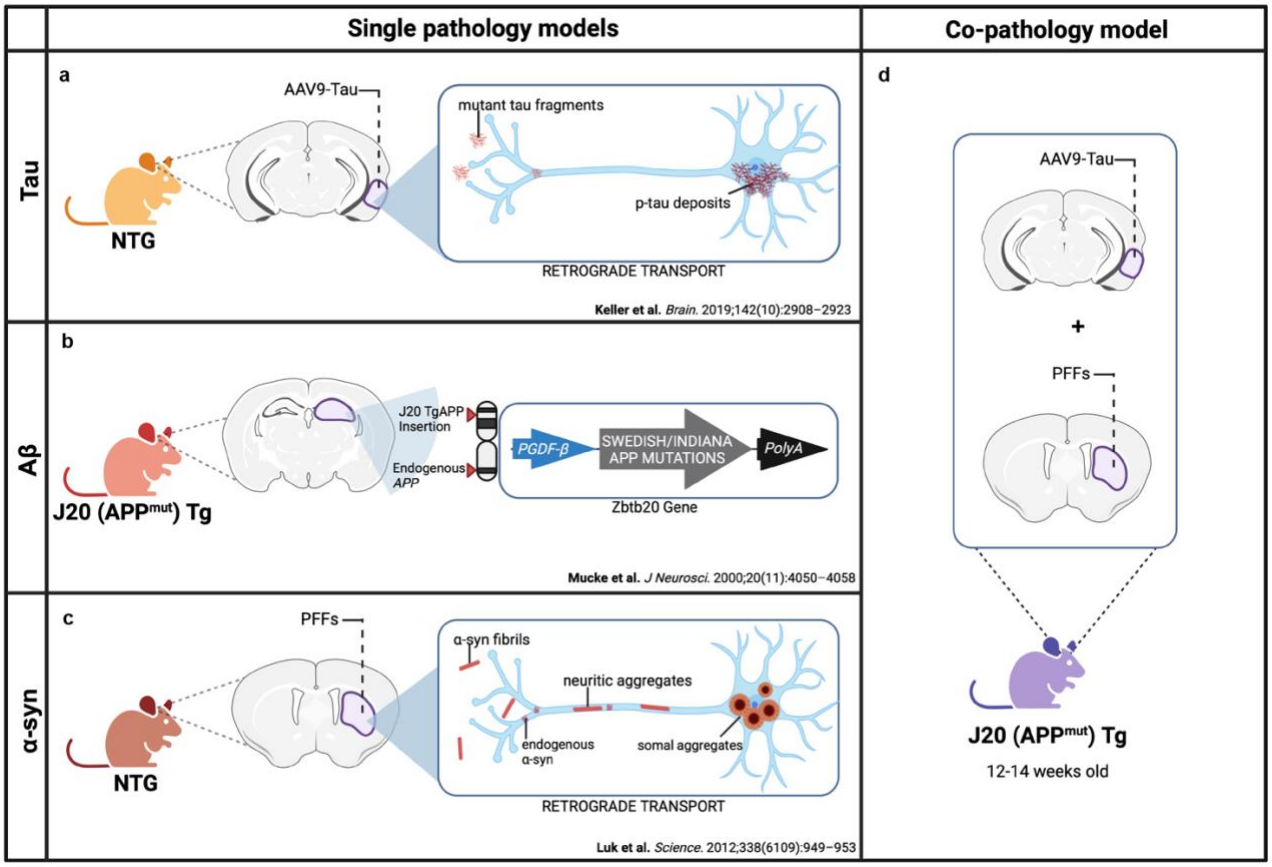

754

755 **Figure 1. Strategy for creating co-pathology mouse model.** At 12-14 weeks old, non-transgenic
756 (NTG) wild-type or J20 APP mutant (APP^{mut}) transgenic (Tg) age-matched males and females are
757 used to induce either single pathology controls or the co-pathology model in vivo. (a) For τau
758 single pathology controls, NTG mice received injections of 2μL of 3.2E12 vg/mL AAV9-Tau into
759 the entorhinal cortex. This viral overexpression of mutant tau results in the accumulation of
760 phosphorylated tau (p-tau) in the cell body via retrograde transport. (b) For Aβ pathology, J20 Tg
761 mice expressing human APP with Swedish and Indiana mutations under the PGDF-β promoter
762 were used. These mice develop Aβ plaques due to overproduction and deposition of Aβ. (c) For
763 α-syn pathology in the PFF single pathology control, NTG mice were injected with 2μL of 5μg α-
764 syn PFFs into the striatum. Fibrils deposited into the brain will interact with endogenous α-syn
765 within the neurons to form neuritic and somal aggregates. (d) For the co-pathology model, J20 Tg

766 mice received both AAV9-Tau and α-syn PFFs into the entorhinal cortex and striatum,
767 respectively, to simultaneously induce the expression of Aβ, tau and α-syn the brain.
768
769
770
771
772
773
774
775
776
777
778
779
780
781
782
783

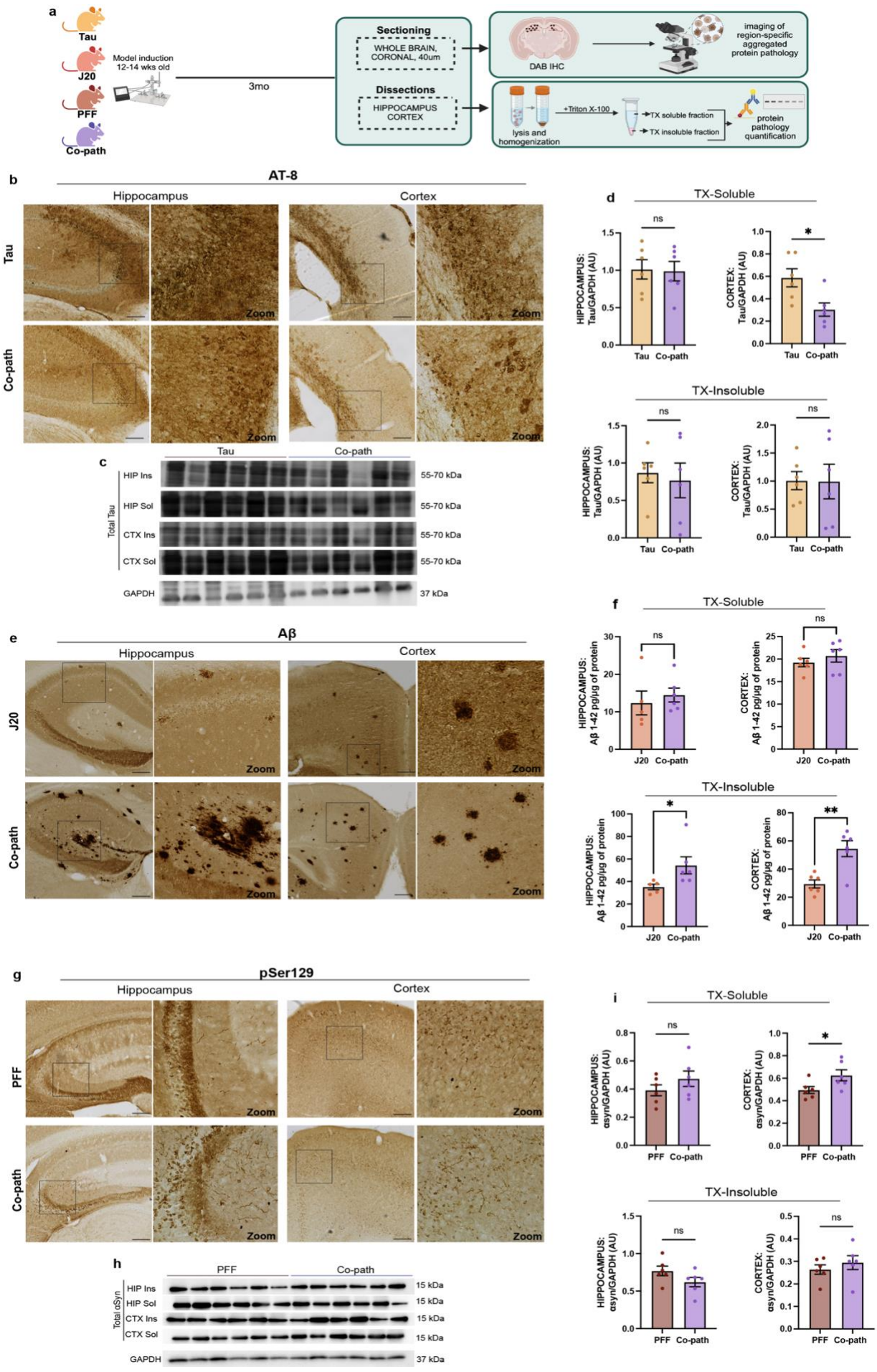
a
Tau
J20
PFF
Co-path
Model induction
12-14 wks old
3mo
Sectioning
WHOLE BRAIN, CORONAL, 40um
Dissections
HIPPOCAMPUS CORTEX
DAB IHC
imaging of region-specific aggregated protein pathology
lysis and homogenization
+Triton X-100
TX soluble fraction
TX insoluble fraction
protein pathology quantification
b
AT-8
Hippocampus
Cortex
Tau
Co-path
Zoom
c
Tau
Co-path
HIP Ins
HIP Sol
CTX Ins
CTX Sol
Total Tau
55-70 kDa
GAPDH
37 kDa
d
TX-Soluble
TX-Insoluble
HIPPOCAMPUS: Tau/GAPDH (AU)
CORTEX: Tau/GAPDH (AU)
ns
*
e
Aβ
J20
f
HIPPOCAMPUS: Aβ 1-42 pg/µg of protein
CORTEX: Aβ 1-42 pg/µg of protein
**
g
pSer129
PFF
h
Total αSyn
15 kDa
i
HIPPOCAMPUS: αsyn/GAPDH (AU)
CORTEX: αsyn/GAPDH (AU)

785 **Figure 2. The presence of co-pathology enhances Aβ and α-syn pathology load in**
786 **hippocampus and cortex.** (a) 12–14-week-old animals were induced with either single
787 pathologies or co-pathologies. At 3mpi, mice were sacrificed and brains processed for IHC or
788 biochemical analysis of protein levels. (b) AT-8/pTau-positive neurons (DAB+, brown) in the
789 hippocampus and cortex of tau single pathology and co-pathology brains. (c) Representative
790 immunoblot of total tau and GAPDH. Blots are cropped from original images found in Extended
791 Data figures. (d) Quantification of tau protein levels normalized to GAPDH levels in TX-soluble
792 and TX-insoluble hippocampus and cortical samples from Tau single pathology and co-pathology
793 mice. (e) Aβ-positive plaques (DAB+, brown) expressed within the hippocampus and cortex of
794 J20 single pathology (Aβ) and co-pathology brains. (f) ELISA was used to quantify Aβ1-42 levels
795 in the brains of J20 single pathology and co-pathology mice. Triton-X100 soluble and insoluble
796 fractions of hippocampal and cortical tissue were used. (g) pSer129-positive inclusions in the
797 hippocampus and cortex of PFF only (α-syn) and co-pathology brains. (h) Representative
798 immunoblot of total α-syn and GAPDH. Blots are cropped from original images found in Extended
799 Data figures. (i) Quantification of synuclein protein levels normalized to GAPDH levels in TX-
800 soluble and TX-insoluble hippocampus and cortical samples from PFF single pathology and co-
801 pathology mice. All images taken at 10X or 20X for zooms, scale bars = 100μm. Analyzed using
802 Welch's t-test. *$p<0.05$, **$p<0.01$. n=6 animals per group, both males and females used.
803
804
805
806
807

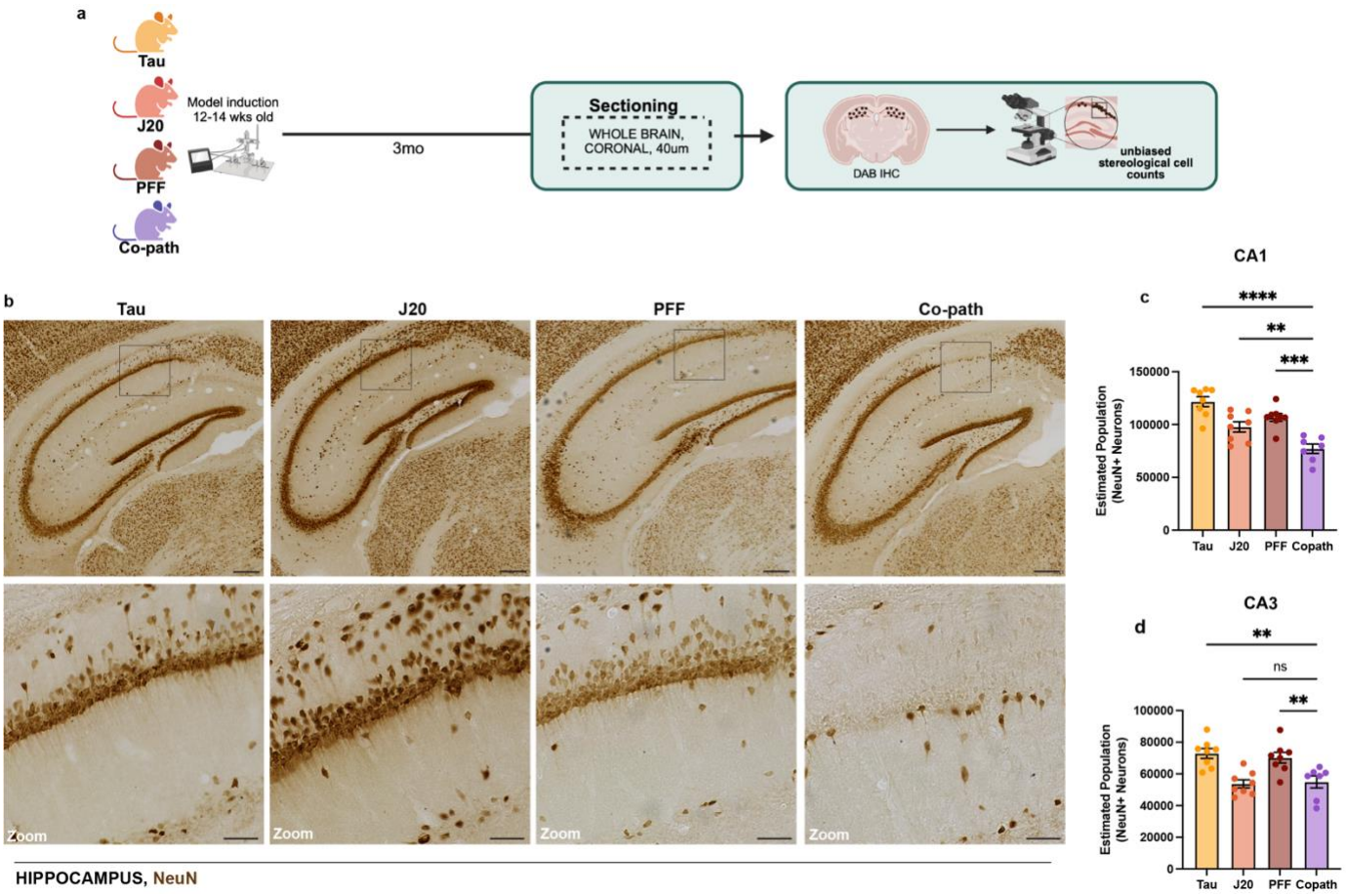

Figure 3. Co-pathologies drive neurodegeneration in the hippocampus at 6mpi. (a) At 3mpi single pathology and co-pathology brains were processed for DAB IHC and unbiased stereology. (b) Representative brightfield images of NeuN+ neurons (DAB+, brown) in the hippocampus of Tau, J20 and PFF single pathology and co-pathology brain. Unbiased stereology was used to quantify the number of NeuN+ neurons in the (c) CA1 and (d) CA3 regions of the hippocampus in the co-pathology mouse model compared to Tau, J20 and PFF single pathology brains. (All images taken at 20X. Scale bars = 300µm and 100µm for zooms. One-way ANOVA with post hoc test was used to assess for significance. Mean values +/- SEM are plotted. ns = no significance, **p<0.01, ***p<0.005, ****p<0.0001. n=7-8 animals per group, both males and females used.

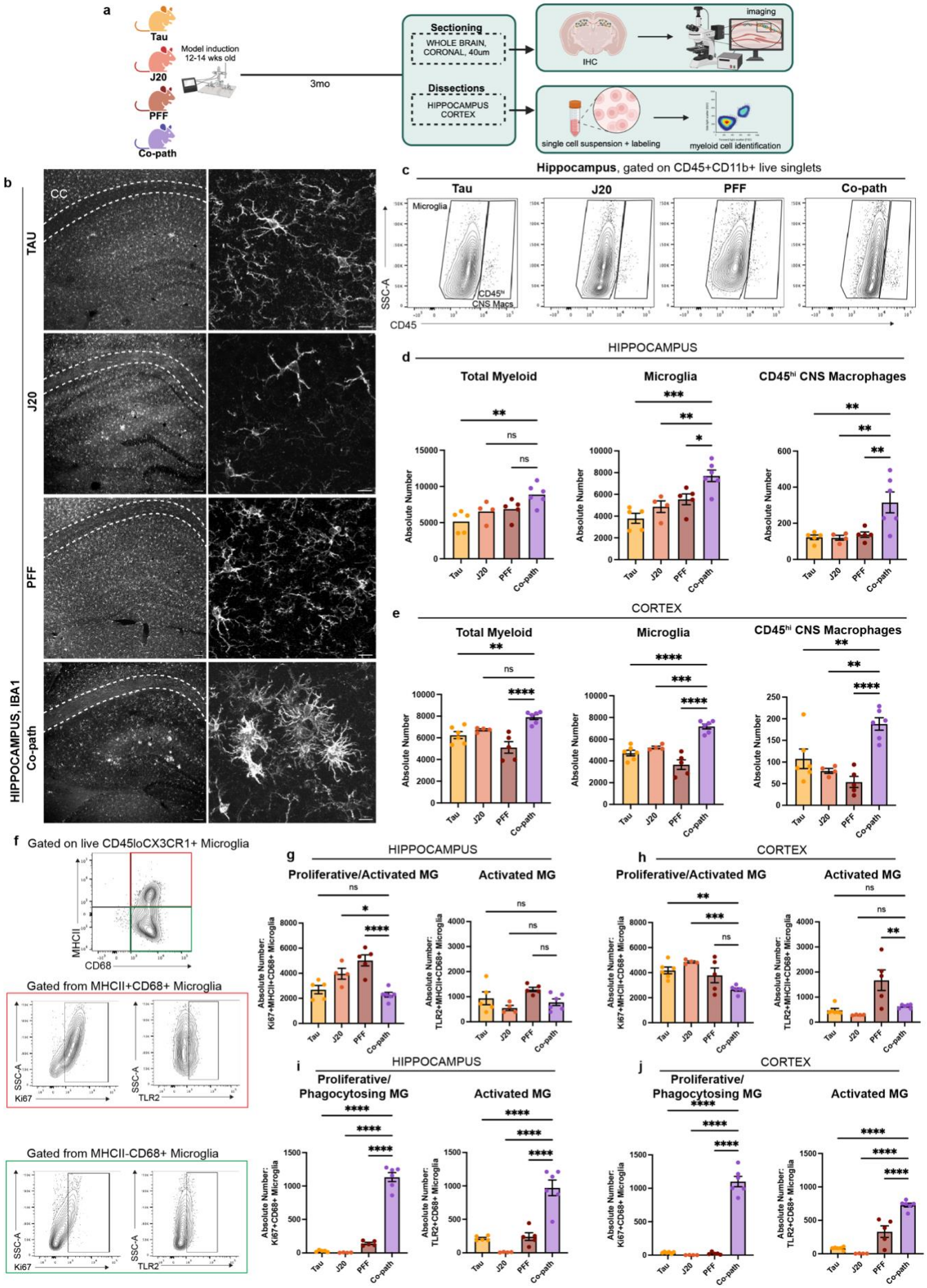
a
Tau
J20
PFF
Co-path
Model induction
12-14 wks old
3mo
Sectioning
WHOLE BRAIN, CORONAL, 40um
Dissections
HIPPOCAMPUS CORTEX
IHC
imaging
single cell suspension + labeling
myeloid cell identification
b
HIPPOCAMPUS, IBA1
TAU
J20
PFF
Co-path
CC
c
Hippocampus, gated on CD45+CD11b+ live singlets
Tau
J20
PFF
Co-path
Microglia
CD45hi CNS Macs
SSC-A
CD45
d
HIPPOCAMPUS
Total Myeloid
Microglia
CD45hi CNS Macrophages
Absolute Number
e
CORTEX
Total Myeloid
Microglia
CD45hi CNS Macrophages
f
Gated on live CD45loCX3CR1+ Microglia
MHCII
CD68
Gated from MHCII+CD68+ Microglia
Ki67
TLR2
Gated from MHCII-CD68+ Microglia
g
HIPPOCAMPUS
Proliferative/Activated MG
Activated MG
Absolute Number: Ki67+MHCII+CD68+ Microglia
Absolute Number: TLR2+MHCII+CD68+ Microglia
h
CORTEX
Proliferative/Activated MG
Activated MG
i
HIPPOCAMPUS
Proliferative/ Phagocytosing MG
Activated MG
Absolute Number: Ki67+CD68+ Microglia
Absolute Number: TLR2+CD68+ Microglia
j
CORTEX
Proliferative/ Phagocytosing MG
Activated MG

821 **Figure 4. Co-pathologies enhance microglia activation at 3mpi.** (a) J20 transgenic mice are
822 injected at 12-14 weeks of age with 2uL of 5ug α-syn PFFs and 2uL of 3.2E12 vg/mL AAV9-Tau
823 into the striatum and entorhinal cortex, respectively. For single pathology controls, age-matched
824 non-transgenic littermates are injected with α-syn PFFs into the dorsal lateral striatum for PFF
825 single pathology control or AAV9- Tau into the entorhinal cortex for Tau single pathology control.
826 Age-matched J20 mice are used as the Aβ single pathology controls. At 3mpi, brains were
827 collected and the hippocampus and surrounding cortices dissected and processed for spectral flow
828 cytometry. (b) Representative fluorescent grayscale images of Iba1+ microglia in the hippocampus
829 of Tau, J20 and PFF single pathology controls compared to that in the co-pathology model. (c)
830 Representative flow cytometry contour plots showing $CD45^{mid\text{-}lo}$ microglia and $CD45^{hi}$ CNS
831 macrophages in single pathology and co-pathology hippocampus. The relative frequency of total
832 myeloid cells, microglia and $CD45^{hi}$ infiltrating monocytes and resident macrophages in the (d)
833 hippocampus and (e) cortex of Tau, J20 and PFF only compared to co-pathology brains are plotted.
834 (f) From the $CD45^{mid\text{-}lo}$ microglia population, representative contour plots show expression of
835 activation markers MHCII (antigen presentation, activated), CD68 (phagocytosing). The absolute
836 number of $MHCII^{+}CD68^{+}$ microglia that are $Ki67^{+}$ or $TLR2^{+}$ in the (g) hippocampus and (b) cortex
837 of co-pathology and single pathology mice. $MHCII^{-}CD68^{+}$ microglia that are $Ki67^{+}$ or $TLR2^{+}$ in
838 the (i) hippocampus and (j) cortex Tau, J20 and PFF only compared to co-pathology brains are
839 plotted. Analyzed using One-way ANOVA. Mean values +/- SEM are plotted. *$p<0.05$, **$p<0.01$,
840 ***$p<0.005$. n=5-6/group, with two brain regions pooled per sampled, both males and females
841 included in analysis. First panel images taken at 10X magnification and zoomed, z-stack images
842 at 40X. Scale bars (10X) = 100μm, scale bars (40X) = 10μm.

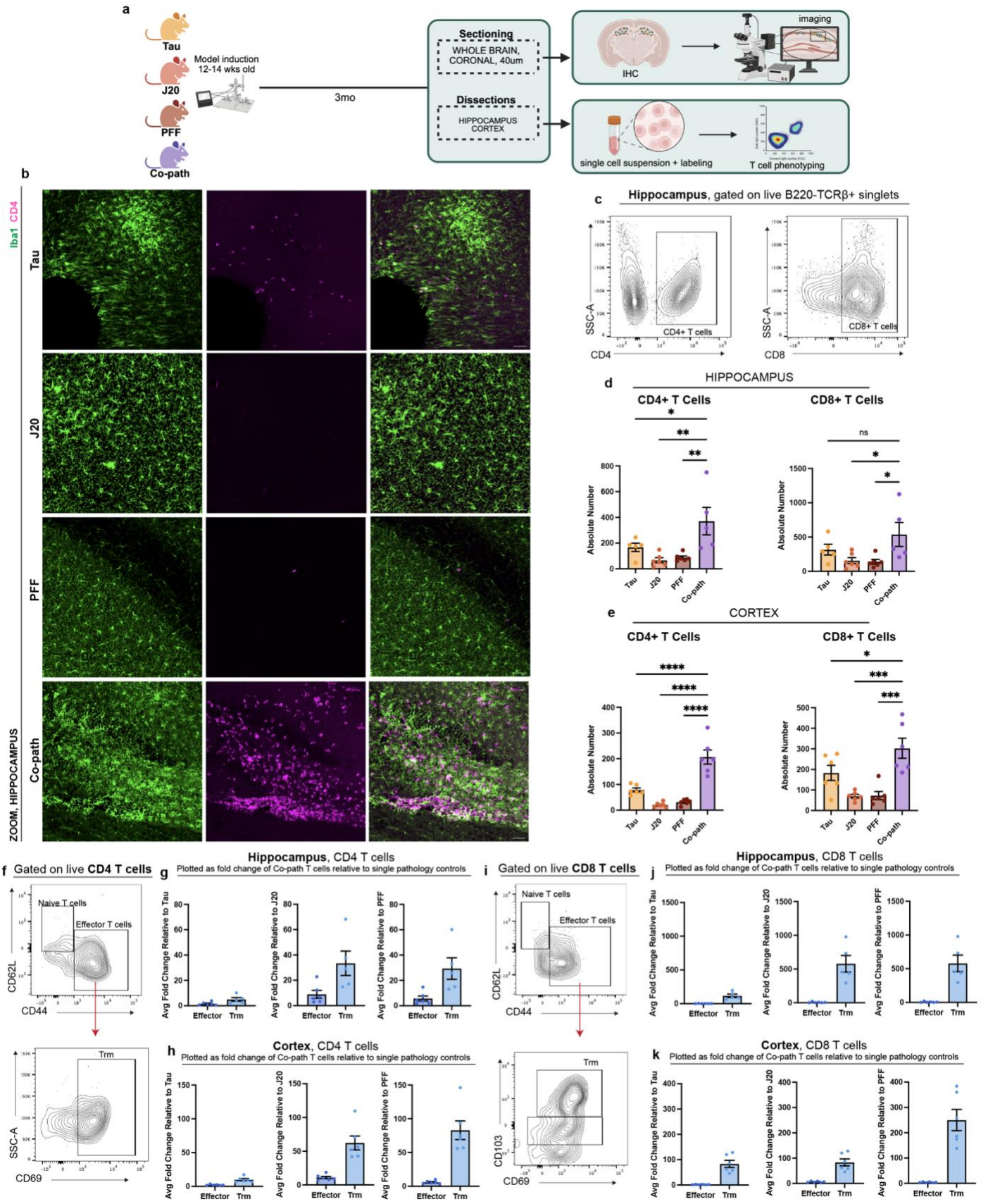
a
Tau
J20
PFF
Co-path
Model induction
12-14 wks old
3mo
Sectioning
WHOLE BRAIN, CORONAL, 40um
Dissections
HIPPOCAMPUS CORTEX
IHC
imaging
single cell suspension + labeling
T cell phenotyping
b
Iba1 CD4
ZOOM, HIPPOCAMPUS
c
Hippocampus, gated on live B220-TCRβ+ singlets
SSC-A
CD4+ T cells
CD4
CD8+ T cells
CD8
d
HIPPOCAMPUS
CD4+ T Cells
CD8+ T Cells
Absolute Number
ns
e
CORTEX
f
Gated on live CD4 T cells
Naive T cells
Effector T cells
CD62L
CD44
Trm
CD69
g
Hippocampus, CD4 T cells
Plotted as fold change of Co-path T cells relative to single pathology controls
Avg Fold Change Relative to Tau
Avg Fold Change Relative to J20
Avg Fold Change Relative to PFF
Effector
Trm
h
Cortex, CD4 T cells
i
Gated on live CD8 T cells
CD103
j
Hippocampus, CD8 T cells
k
Cortex, CD8 T cells

843

844 **Figure 5. Co-pathologies promote T cell responses and tissue-resident memory T cell**
845 **phenotypes at 3mpi.** (a) J20 transgenic mice are injected at 12-14 weeks of age with 2uL of 5ug
846 α-syn PFFs and 2uL of 3.2E12 vg/mL AAV9-Tau into the striatum and entorhinal cortex,
847 respectively. For single pathology controls, age-matched non-transgenic littermates are injected
848 with α-syn PFFs into the dorsal lateral striatum for PFF single pathology control or AAV9- Tau
849 into the entorhinal cortex for Tau single pathology control. Age-matched J20 mice are used as the
850 Aβ single pathology controls. At 3mpi, brains were collected and the hippocampus and
851 surrounding cortices dissected and processed for spectral flow cytometry. (b) Representative
852 fluorescent images of Iba1+ microglia (green) and CD4+ T cells (magenta) in the hippocampus of
853 Tau, J20 and PFF single pathology controls compared to that in the co-pathology model. (c)
854 Representative flow cytometry contour plots show proportion for CD4+ and CD8+ T cells. The
855 relative frequency of CD4+ and CD8+ T cells in the (d) hippocampus and (e) cortex of Tau, J20
856 and PFF only compared to co-pathology brains are plotted. (f) Representative contour plot showing
857 expression and gating scheme of CD4+ Trm T cells. Quantified average fold change of CD44+
858 effector and CD69+ Trm in co-pathology (g) hippocampus and (h) cortex relative to Tau, J20 and
859 PFF single pathologies. (i) Representative contour plot showing expression and gating scheme of
860 CD8+ Trm T cells. Quantified average fold change of CD44+ effector and CD69+CD103+ Trm
861 in co-pathology (j) hippocampus and (k) cortex relative to Tau, J20 and PFF single pathologies.
862 Analyzed using One-way ANOVA. Mean values +/- SEM are plotted. *$p<0.05$, **$p<0.01$,
863 ***$p<0.005$. n=6/group, with two brain regions pooled per sampled, both males and females
864 included in analysis. All images taken at 10X magnification with z-stack, and digitally zoomed
865 using Nikon Elements software. Scale bars = 50μm.

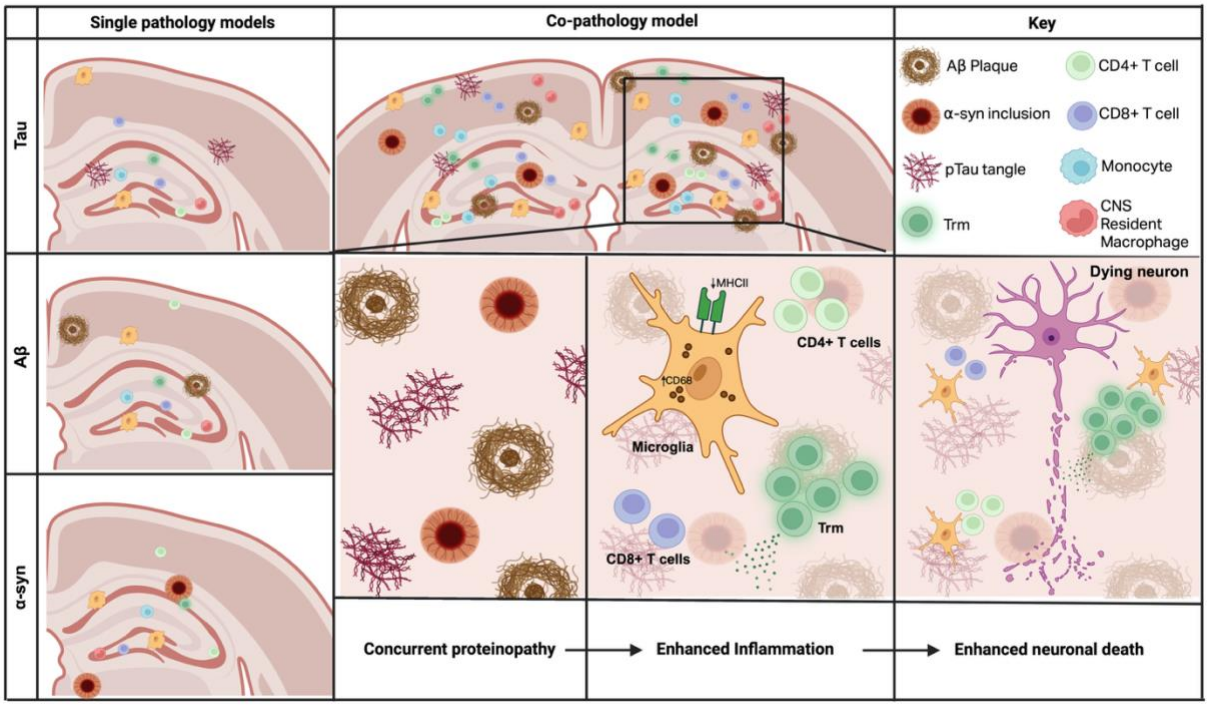

Figure 6. Synergistic effects of co-pathologies promote neuroinflammation, protein pathology load and neurodegeneration. Single pathology models (left panel) showing relatively mild immune activation and pathology, with little to no inclusion of tissue-resident memory (Trm) T cells, CD4+ and CD8+ T cells, monocytes and CNS resident macrophages. With the co-pathology model (middle panels), we demonstrate that concurrent protein aggregation (Aβ plaques, p-tau tangles and α-syn inclusions synergistically lead to increased recruitment and expansion of CNS-infiltrating immune cells and Trm populations. This is accompanied by microglial phenotype changes and elevated CD68+ expression and decreased number of MHCII+ cells. The cumulative effects of aggregated protein burden and chronic neuroinflammation result in neuronal damage and subsequent death.

880 # Methods

881 **Mice**

882 The mouse strain used for this research project, B6J.Cg-*Zbtb20*$^{Tg(PDGFB\text{-}APPSwInd)20Lms}$/Mmjax,
883 (RRID:MMRRC_034836-JAX), was obtained from the Mutant Mouse Resource and Research
884 Center (MMRRC) at The Jackson Laboratory, an NIH-funded strain repository, and was donated
885 to the MMRRC by Lennart Mucke, Ph.D., Gladstone Institute of Neurological Disease. Age and
886 sex-matched non-transgenic littermates (NTG, C57BL/6J background) were used for Sham and
887 single pathology induction. For all experiments presented, both male and female mice were used.
888 All research conducted on animals was approved by the Institutional Animal Care and Use
889 Committee at the University of Alabama at Birmingham and methods followed the Animal
890 Research: Reporting of *In vivo* Experiments (ARRIVE) 2.0 guidelines (arriveguidelines.org).

891

892 **Fibril and viral vector generation**

893 *Mouse α-synuclein pre-formed fibrils*

894 α-syn mouse pre formed fibrils (PFFs) were generated and purified from mouse α-synuclein from
895 the Volpicelli-Daley lab at the University of Alabama at Birmingham according to previously
896 published protocols [102,103]. Briefly, mouse PFFs were thawed and aliquoted into 25uL (5mg/mL)
897 and transferred to polystyrene sonication tubes. Tubes containing PFFs were then transferred to a
898 Q700 Sonicator water reservoir once the water was at 10C. Fibrils were sonicated for 15 minutes,
899 with pulse on and off durations, at a power of approximately 110 watts per pulse. After sonication,
900 tubes are quickly spun down and 1uL of sonicated PFFs transferred into an Eppendorf tube in 1X
901 PBS, for a final volume of 500uL. 5uL of this solution is sent for dynamic light scattering analysis
902 to check for PFF fragmentation of around 50nm after sonication.

903

904 *AAV9-Tau virus*

905 AAV double mutant (dbl^{mut}) tau (AAV9-Tau) genome plasmid was engineered by standard cloning
906 techniques to express human tau (2N4R isoform) encoding P301L/S320F mutations driven by the
907 hybrid chicken β-actin promoter and flanked by AAV2 iTRs. [104]. Recombinant adeno-associated
908 virus capsid 9 (AAV9) vectors were generated as described in prior studies[105]. Briefly, HEK293
909 cells were co-transfected with either dbl^{mut} tau or green fluorescent protein (GFP) genome
910 plasmids, together with plasmids encoding AAV rep/cap genes and adenovirus helper proteins.
911 AAV viral capsids were purified from cells and culture media by iodixanol gradient centrifugation,
912 followed by dialysis in Dulbecco's PBS containing calcium and magnesium. Titers were
913 determined by ddPCR using primers for the AAV iTRs and normalized to 3.2 viral genomes per
914 mL (vg/mL).

915

916 **Stereotaxic injections**

917 Mice aged 12-14 weeks old were deeply anesthetized using an isoflurane vaporizing instrument
918 (UAB Animal Resource Program) and immobilized to a stereotaxic frame (Stoelting) on top of a
919 heating pad to ensure appropriate internal body temperature is maintained. 26s/2"/2 10µL
920 Hamilton syringes along with an automatic injecting system (Stoelting) are used to unilaterally
921 (immunohistochemistry, DAB and fluorescence) or bilaterally (behavior, flow cytometry) inject
922 2uL of mouse α-syn PFFs (5µg/mL), mouse α-syn monomer (5µg/mL), AAV9-dbl^{mut} tau virus
923 (3.2E12vg/mL) or AAV9-GFP (3.2E12vg/mL). PFFs or monomer control were injected into the
924 dorsal lateral striatum based on bregma (AP +0.5mm, ML +/-2.0mm and DV -3.0mm from the
925 dura) AAV9-Tau or AAV9-eGFP viruses were injected into the entorhinal cortex (AP -3.5mm,

926 ML +/-3.9mm and DV -4.2mm from dura). Injection needle was left in the injection site for an
927 additional 2 minutes following completion and then slowly retracted from the site over the course
928 of another 2 minutes. All surgical protocols and post-surgery aftercare methods were followed and
929 approved by the Institutional Animal Care and Use Committee at the University of Alabama at
930 Birmingham.
931 To induce the co-pathology model, 3-month-old J20 transgenic mice were injected with mouse α-
932 syn PFFs into the striatum and AAV9-Tau virus into the entorhinal cortex. For sham surgery, non-
933 transgenic (NTG) littermates were injected with mouse α-syn monomer and AAV9-eGFP into the
934 striatum and entorhinal cortex, respectively.
935 To induce single pathology controls, NTG mice were injected with mouse α-syn PFFs into the
936 dorsal lateral striatum for α-syn models and AAV9-Tau virus into the entorhinal cortex for tau
937 models. α-syn monomer into the striatum and AAV9-GFP were injected into the dorsal lateral
938 striatum and entorhinal cortex, respectively, of non-transgenic mice as controls. J20 transgenic
939 mice were used as the Aβ single pathology mice, compared to un-injected NTG littermates.
940
941 **Tissue preparation and processing**
942 At 3 months post-induction (3mpi) and 6 months post-induction (6mpi) of the co-pathology model
943 and single-color controls, mice were anesthetized using isoflurane and transcardially perfused with
944 0.01M phosphate-buffered saline (PBS, pH = 7.4) and fixed with 4% paraformaldehyde (PFA in
945 PBS, pH = 7.4). Brains were then dissected and incubated in 4% PFA for 2 hours at room
946 temperature. After fixation, brains were placed in 30% sucrose in PBS for 3 days until brains were
947 fully saturated. Brains were then frozen on dry ice and cryosectioned coronally at 40μm on a

948 sliding microtome (Thermo Scientific Micron HM 450). Sliced brain tissue was then stored in a
949 50% glycerol/PBS solution at -20°C.
950
951 **Immunofluorescent immunohistochemistry**
952 Free-floating 40-µm thick sections were washed in 0.01M tris-buffered saline solution (TBS, pH
953 7.4) prior to an antigen retrieval process with a solution of 10mM sodium citrate and 0.05% Tween-
954 20 in TBS. Sections were then incubated in 5% blocking serum at room temperature before being
955 incubated overnight in the following primary antibody solutions (TBST, 1% serum): anti-CD4
956 (clone RM4-5, ThermoFisher), anti-CD8 (clone 4SM15, eBioscience) and anti-Iba1 (WACO). On
957 the following day, sections were washed in TBS with .1% Triton-100 and incubated in fluorescent
958 conjugated antibody in the dark for 2 hours at room temperature. Sections were then washed in
959 TBST and mounted on microscope slides for analysis. Slides were imaged at 20X on a Nikon A1
960 Laser Scanning Confocal microscope.
961
962 **DAB immunohistochemistry**
963 Free-floating 40-µm thick sections were washed in 0.01M tris-buffered saline solution (TBS, pH
964 7.4) prior to being quenched with 3% hydrogen peroxide in TBS for 5 minutes. Next, sections
965 underwent an antigen retrieval process with a solution of 10mM sodium citrate and 0.05% Tween-
966 20 in TBS for 30 minutes at 37°C. Following this, sections were blocked in a 5% goat or donkey
967 serum solution for at least 1 hour at room temperature and then incubated overnight at 4°C with
968 the following antibodies in 1% serum solution: anti-CD3 (clone 17A2, eBioscience), anti-tyrosine
969 hydroxylase (clone: EP1536Y, Abcam), anti-alpha synuclein, phosphor-serine 129 (pSer129, close
970 EP1536Y, Abcam), anti-AT8 (clone MN1020, ThermoFisher), anti-Aβ (clone D54D2, Cell

971 Signaling) and anti-NeuN (clone EPR12763, Abcam). Sections were then incubated with a
972 biotinylated secondary antibody (1:1000, Vector Labs) in a 1% serum in TBST solution. After
973 incubation, sections were washed with TBS and incubated in the Vectastain ABC Reagent (Vector
974 Labs) for 30 minutes at RT prior to development with the Vectastain diaminobenzidine DAB Kit
975 (SK-4199, Vector Labs) according to the manufacturer's protocol. Sections were then mounted
976 onto plus-coated slides and dehydrated with a gradient of ethanol solutions (70%-100%) followed
977 by Citrisolv. Slides were them coverslipped with Permount Mounting Media (Electron Microscopy
978 Sciences). Slides were then images at 10X and 20X on a Zeiss Imager M2 brightfield microscope
979 (MBF Biosciences).
980
981 **Unbiased stereology of the hippocampus and substantia nigra pars compacta**
982 In order to quantify neuronal cell loss, an unbiased stereology protocol was used. TH and NeuN-
983 DAB stained (see 'DAB Immunohistochemistry' section) SNpc and hippocampal tissue sections,
984 respectively, were imaged and analyzed with a Zeiss Axio Imager M2 microscope (MBF
985 Biosciences) and the Cavalieri stereology probe used to count cells, with a section thickness of
986 25µm to account for dehydration of sections. To quantify NeuN+ neurons in the hippocampus,
987 contours were drawn around the five to seven sections, focusing on the CA1 and CA3 regions. To
988 quantify Th+ neurons in the SNpc, contours were drawn around both sides of the nigra, in four to
989 five sections. Similar contours were drawn in the nigra to quantify α-syn+ neurons. For
990 stereological counting, the grid size used for the hippocampus was 130µmx130µm and the
991 counting frame was 40µmx40µm. In the SNpc, the grid size and counting frame were, 100x100
992 and 50µmx50µm, respectively.
993

994 **Brain single cell isolation and flow cytometry**

995 At 3mpi, co-pathology and single pathology mice were anesthetized and transcardially perfused
996 with 0.01M PBS (pH 7.4). Briefly, brain tissue was removed and the brain regions dissected.
997 Tissue was then digested with 1 mg/mL Collagenase IV (Sigma) diluted in RPMI 1640 (1X,
998 Gibco). Following enzyme digestion, tissue was then filtered and smashed through a 70μm filter
999 using a syringe plunger and mononuclear cells isolated out using a 30/70% Percoll gradient (GE).
1000

1001 For cell staining, isolated brain cells were blocked with anti-Fcγ receptor (1:100, Biosciences).
1002 Following this, cell surface markers were labelled with the following, fluorescent-conjugated
1003 antibodies against CD45 (clone 30-F11, eBioscience), CD11b (clone M1/70, BioLegend), MHCII
1004 (M5/114.15.2, BioLegend), Ly6C (clone HK 1.4, BioLegend), TCRβ (clone H57-597, Biolegend),
1005 CD4 (GK1.5, BioLegend), CD8a (clone 53-6.7, BioLegend). CD69 (clone H1.2F3, BioLegend), ,
1006 B220 (clone RA3-6B2, BD Biosciences), CD44 (clone IM7, Biolegend), CD62L (clone MEL-14,
1007 BioLegend), CD103 (clone 2E7, BioLegend), TLR2 (clone CB225, BD Biosciences), Ki67 (clone
1008 16A8, BioLegend), CX3CR1 (clone SA011F11, BioLegend), CD68 (clone FA-11, BioLegend). A
1009 fixable viability dye was used to distinguish live cells, per the manufacturer's protocol Aqua-
1010 LIVE/DEAD Stain Kit (Invitrogen). As single-color compensation controls, isolated splenocytes
1011 or UltraComp eBeads™ (Invitrogen) were used. To analyze and run samples, a BD Symphony
1012 (BD Biosciences) or Spectral Enabled Symphony flow cytometer were used at the UAB Flow
1013 Cytometry and Single Cell Core Facility. Mean cell counts, percentages and mean fluorescent
1014 intensity were measured and analyzed using FlowJo (Tree Star) software.
1015

1016 **Mouse brain lysate preparation**

1017 Brain tissue was micro dissected, snap frozen in super-cooled bath of 2-methylbutane with dry ice,
1018 and stored at -80°C. Tissue lysates were homogenized with a tissue grinder using 20%
1019 weight/volume lysis buffer (50 mmol/L Tris-HCl pH 7.4, 175 mmol/L NaCl, 5 mmol/L EDTA)
1020 supplemented with protease and phosphatase inhibitors and sonicated for 10 sec on ice. After
1021 addition of Triton X-100 to a final concentration of 1% volume/volume, samples were incubated
1022 on ice for 30 minutes and centrifuged at 15,000 xg for 60 min at 4°C. The supernatant was saved
1023 as the Triton X-100 soluble fraction. The pellet was resuspended in lysis buffer with 2% SDS,
1024 sonicated for 10 sec, and centrifuged for 10 minutes at 15,000 xg. The resulting supernatant was
1025 reserved as the Triton X-100 insoluble fraction. Protein concentration was determined by the
1026 bicinchoninic acid assay (Pierce Cat# 23225).
1027
1028 **Amyloid β detection by Aβ1-42 ELISA**
1029 A total of 20 µg brain lysate was used to measure concentration of Aβ1-42 with the human
1030 Amyloid beta (aa1-42) Quantikine ELISA (R&D Systems Cat# DAB142) kit following the
1031 manufacturer's protocol. Colorimetric signal was measured using the SpectraMax iD3 (Molecular
1032 Devices).
1033
1034 **Western Blot**
1035 *Chemiluminescence*
1036 A total of 20µg of protein from the Triton X-100 soluble and insoluble fractions described above
1037 were denatured in dithiothreitol (DTT) buffer (0.25 M Tris-HCl pH 6.8, 200mM DTT, 8% SDS,
1038 30% glycerol, 2mg bromophenol blue) by boiling for 10m. Samples were run on 15% SDS-
1039 polyacrylamide gels and transferred onto nitrocellulose membranes, which were then fixed for

1040 30m in 0.4% paraformaldehyde. Blots were blocked in 5% dry milk in TBS-T for 1 hour at ambient
1041 temperatures and incubated in primary antibodies at 4ºC overnight. Primary antibody
1042 concentrations are as follows: Alpha-Synuclein (1:1000; BD-Biosciences 610787) and GAPDH
1043 (1:10,000; Cell Signaling 14C10). Blots were washed in TBS-T, incubated in HRP-conjugated
1044 secondary antibodies (Mouse HRP: Jackson Labs 115-035-003; Rabbit HRP: Jackson Labs 111-
1045 035-003) at 1:2000 for 1h at ambient temperatures, and imaged using a BioRad ChemiDoc MP
1046 system. Blots were analyzed using BioRad Image Lab software.

1047 *Fluorescence*

1048 Blots were run as described above. LI-COR blocking buffer and antibody diluents (LI-COR 927-
1049 66003) were used with Tau (1:1000; Cell Signaling 43984S) and GAPDH antibodies. IRDye-
1050 conjugated secondary antibodies (Mouse IRDye 680: LI-COR 926-68070; Rabbit IRDye 800: LI-
1051 COR 926-32211) were used at 1:2000 for 1h at ambient temperatures. Blots were imaged using a
1052 LI-COR Odyssey CLx system and analyzed using LI-COR Image studio software.

1053

1054 **Dendritic spine morphology analysis**

1055 *Perfusions and brain tissue processing*

1056 For iontophoretic microinjections, mice were anesthetized with Fatal Plus (Vortech
1057 Pharmaceuticals, Catalog #0298-9373-68) and transcardially perfused with cold 1%
1058 paraformaldehyde (PFA; Sigma Aldrich, Catalog #P6148) for 1 min, followed by 4% PFA with
1059 0.125% glutaraldehyde (Fisher Scientific, Catalog #BP2547) for 10 min. A peristaltic pump
1060 (Cole Parmer) was used for consistent administration of cold PFA. Immediately following
1061 perfusion, each brain was extracted and drop-fixed in 4% PFA with 0.125% glutaraldehyde for
1062 8–12 h at 4 °C. After fixation, brains were coronally sliced in 250 µm thick sections using a

1063 Leica vibratome (VT1000S, speed 70, frequency 7). Brains were sliced in 0.1 M PB and stored at
1064 4 °C, one slice per well in a 48-well plate, in 0.1 M PB with 0.1% sodium azide (Fisher, Catalog
1065 #BP922I).
1066
1067 *Iontophoretic microinjections*
1068 Iontophoretic microinjections were performed based on methods described previously[106,107]. A
1069 Nikon Eclipse FN1 upright microscope with a 10× objective and a 40× water objective was
1070 placed on an air table. The tissue chamber used consisted of a 50 × 75 mm plastic base with a
1071 60 × 10 mm petri dish epoxied to the base. A platinum wire was attached so that the ground wire
1072 could be connected to the bath by an alligator clip. The negative terminal of the electric current
1073 source was connected to a glass micropipette filled with 2 μL of 8% Lucifer yellow dye
1074 (ThermoFisher, Catalog#L453). Micropipettes (A-M Systems, Catalog #603500) with highly
1075 tapered tips were pulled fresh at the time of use. A manual micromanipulator was secured on the
1076 air table with magnets that provided a 45° angle for injection. Brain slices were placed into a
1077 small petri dish containing 1× PBS and DAPI for 5 min at room temperature. After incubation in
1078 DAPI, slices were placed on dental wax, and then a piece of filter paper was used to adhere the
1079 tissue. The filter paper was then transferred to the tissue chamber filled with 1× PBS, and
1080 weighted down for stability. The 10× objective was used to visualize advancement of the tip of
1081 the micropipette in X, Y, and Z planes until the tip was just a few micrometers above the tissue.
1082 The 40× objective was then used while advancing the tip into layer 2/3 of the ventral CA1
1083 regions of the hippocampus. Once the microelectrode contacted a neuron, 2 nA of negative
1084 current were applied for 5 min to fill the neuron with Lucifer yellow. After 5 min, the current
1085 was turned off and the micropipette was removed from the neuron. Neuron impalement within

1086 the CA1 occurred randomly in a blind manner. If the entire neuron did not fill with dye after
1087 penetration, the electrode was removed and the neuron was not used for analysis. Multiple
1088 neurons were injected in each hemisphere of each animal. After injection, the filter paper
1089 containing the tissue was moved back into the chamber containing 1× PBS. The tissue was
1090 carefully lifted off the paper and placed on a glass slide with two 125 µm spacers (Electron
1091 Microscopy Sciences, Catalog #70327-20S). Excess PBS was carefully removed with a
1092 Kimwipe, and the tissue was air-dried for 1 min. One drop of Vectashield (Vector Labs, Catalog
1093 #H1000) was added directly to the slice, and the coverslip (Warner, Catalog #64-0716) was
1094 added and sealed with nail polish. Injected tissue was stored at 4 °C in the dark.
1095
1096 *Confocal microscopy*
1097 Confocal microscopy was used to capture images of Lucifer yellow-filled dendrites on pyramidal
1098 neurons in CA1 of the hippocampus. Our methods are based on previously described
1099 methods[107,108], and are detailed as follows. Imaging was performed by a blinded experimenter on
1100 a Nikon (Tokyo, Japan) Ti2 C2 confocal microscope, using a Plan Apo 60×/1.40 NA oil-
1101 immersion objective. Three-dimensional z-stacks were obtained of secondary dendrites from
1102 dye-impregnated neurons that met the following criteria: (1) within 80 µm working distance of
1103 microscope, (2) relatively parallel with the surface of the coronal section, (3) no overlap with
1104 other branches, (4) located between 40 and 120 µm from the soma. Nikon Elements 4.20.02
1105 image capture software was used to acquire z-stacks with a step size of 0.1 µm, image size of
1106 1024 × 512 px, zoom of 4.8×, line averaging of 4×, and acquisition rate of 1 frame/s.
1107 Confocal microscopy was also used to capture images of slices from mice. Imaging was
1108 performed on a Nikon Ti2 C2 confocal microscope, using a Plan Fluor 10×/0.75 NA air

1109 objective. Nikon Elements 4.20.02 image capture software was used to acquire stitched images
1110 (20 × 10 field) by automatically stitching multiple adjacent 10× images using 25% blending
1111 overlap. Each frame had an image size of 1024 × 1024 px, and acquisition rate of 1 frame/s.
1112 Subsequently, 10× stitched images were acquired, with all other imaging parameters remaining
1113 the same. Following image acquisition, post-image processing was performed using Fiji ImageJ.
1114 Each image file was a two channel image. The Split Channels function was used to separate the
1115 two channels.
1116
1117 *Dendritic spine morphometry analysis*
1118 Confocal z-stacks of dendrites were deconvolved using Huygens Deconvolution System (16.05,
1119 Scientific Volume Imaging, the Netherlands). The following settings were used: deconvolution
1120 algorithm: GMLE; maximum iterations: 10; signal to noise ratio: 15; quality: 0.003.
1121 Deconvolved images were saved in .tif format. Deconvolved image stacks were imported into
1122 Neurolucida 360 (2.70.1, MBF Biosciences, Williston, Vermont) for dendritic spine analysis. For
1123 each image, the semi-automatic directional kernel algorithm was used to trace the dendrite. The
1124 outer 5 µm of each dendrite were excluded from the trace. All assigned points were examined to
1125 ensure they matched the dendrite diameter and position in X, Y, and Z planes, and were adjusted
1126 if necessary. Dendritic spine reconstruction was performed automatically using a voxel-
1127 clustering algorithm, with the following parameters: outer range = 5 µm, minimum
1128 height = 0.3 µm, detector sensitivity = 80%, minimum count = 8 voxels. The semi-automatically
1129 identified spines were examined to ensure that all identified spines were real, and that all existing
1130 spines had been identified. If necessary, spines were added by increasing the detector sensitivity.
1131 Additionally, merge and slice tools were used to correct errors made in the morphology and

1132 backbone points of each spine. Each dendritic spine was automatically classified as a dendritic
1133 filopodium, thin spine, stubby spine, or mushroom spine based on constant parameters[106,107].
1134 Three-dimensional dendrite reconstructions were exported to Neurolucida Explorer (2.70.1,
1135 MBF Biosciences, Williston, Vermont) for branched structure analysis, which provides
1136 measurements of dendrite length; number of spines; spine length; number of thin, stubby, and
1137 mushroom spines, and filopodia; spine head diameter; and spine neck diameter, among other
1138 measurements. The output was exported to Microsoft Excel (Redmond, WA). Spine density was
1139 calculated as the number of spines per 10 μm of dendrite length. Values per mouse were
1140 calculated by averaging the values for all dendrites corresponding to that mouse. To assess apical
1141 and basal dendrites separately, values for either apical or basal dendrites were averaged per
1142 mouse. For a mouse to be included in statistical analyses for dendritic spine density and
1143 morphology a minimum of 100 μm of dendrite length had to be reconstructed and analyzed.
1144
1145 **Behavior**
1146 Behavior tests to assess for motor and cognitive function were conducted at 6 months post-
1147 induction of co-pathology model or single pathology models. Mice were handled for 3 days prior
1148 to the start of testing and were habituated to the testing room for 1 hour at the start of each testing
1149 day. The order of test was designed to minimize stress to the animals, such that lower-stress tasks
1150 were completed before high-stress tasks. All apparatus was cleaned with 2% chlorohexadine
1151 between trials. The researcher conducting the tests was blinded to experimental groups during
1152 trials and analysis.
1153 *Open Field*

To test for general motor activity, mice were place in a 30.48 x 30.48 cm enclosed field with opaque walls and allowed to explore for 10 minutes. The inner zone was defined as the center of the box. Noldus Average velocity, distance traveled, and percent of the time spent in the center were determined by the Ethovision XT v16 software.

Pole Test

To further test for motor deficits, mice were placed in a dark room and habituated for 1 hour starting at the beginning of the dark phase. Two red lamps were strategically placed in the room to visualize the behavior test without disrupting the dark phase. The pole test was performed using a 53cm wooden dowel rod with a diameter of 10 mm, anchored with a 13.9 x 20 x 1.8 cm block of wood and ridged at 2.54 cm intervals with rolled rubber bands. The dowel rod was placed vertically in the center of a 1x1 foot enclosure. The mice were first trained by being placed face-down at the base of the pole and allowed to climb off onto the floor of the enclosure before being returned to their cage. This training was done twice. Following this, each mouse was placed face-up at the top of the pole and allowed no more than 180 seconds to turn around and climb down to the bottom; this was repeated five times. Mice were given a minimum of 30 seconds to rest between each trial. Three time point measurements were recorded. The first time point started from the time the mouse was placed on the pole to the time taken for the mouse to reach the bottom (total descent time). Measurements were recorded for the time the mouse took to turn around on the pole to face the bottom (turnaround time) and the total time to descend (time descending) in seconds. The average time for each time point was calculated from all five trials for each mouse.

Rotarod

1176 To further test for motor activity, mice were placed on an accelerating rotarod apparatus, and time
1177 taken to fall was measured. Mice were trained on the apparatus over 5 days, with the rotarod speed
1178 increasing from 4 rpm to 40 rpm over 300 seconds. If mice had not fallen by 120 seconds during
1179 the testing trial, the rotation was paused, mouse was removed, and the time was recorded as 120
1180 seconds. Mice underwent two trials per day with 30 minutes of resting time between each trial.
1181
1182 *Barnes Maze*
1183 A blue circular apparatus of 122cm in diameter consisting of forty, five cm, evenly spaced holes
1184 was used throughout the test. The test consisted of three stages: (1) Habituation phase, (2)
1185 Acquisition phase, and (3) Probe phase. The habituation phase took place on day 1 where mice
1186 were placed in the center of the apparatus covered by a black mesh cup uniformly covered. 10
1187 seconds after the placement, mice freely roamed the Barnes maze for an undefined amount of
1188 time until they found and independently entered the escape tunnel. The acquisition phase
1189 occurred through Days 2-6 and consisted of one, five-minute trial. If mice did not find nor enter
1190 the escape tunnel after the five-minute trial, mice were gently guided towards the direction of the
1191 tunnel where they then entered it on their own. Entry into the tunnel was defined as all four paws
1192 in the tunnel. Upon entry, a cover was used to cover to hole to prevent the mice from leaving the
1193 tunnel. The tunnel was then carefully removed from the maze apparatus and gently placed in the
1194 home cage of the mouse. The latency to find and enter the escape tunnel was recorded. On Day
1195 10, mice were again introduced to the maze for one minute without the escape tunnel present.
1196 The amount of time spent in the escape tunnel quadrant, entry zone, and goal box were
1197 determined by the Ethovision XT v16 software.
1198

1199 **Statistical Analysis**

1200 All graphs and subsequent statistical tests were generated using Prism software (GraphPad). Flow
1201 cytometry experiments used ten to twelve independent samples with two brain regions pooled per
1202 sample, for a final number of five to six per group for experiments. Data were analyzed using an
1203 unpaired student's t-test or a one-way ANOVA. Graphs within display the mean +/- SEM. For
1204 unbiased stereology, estimated populations were generated and a one-way ANOVA was used to
1205 determine the significance between groups. *$p<0.05$, **$p<0.01$, ***$p<0.0005$, ****$p<0.0001$.

1206

1207 **Data availability**

1208 The authors affirm that the findings within the manuscript are supported by the data therein. The
1209 data, protocols and key lab materials used and generated in this study are listed in a Key Resource
1210 Table alongside their persistent identifiers on Zenodo (10.5281/zenodo.16739907).

1211

1212 Declarations

1213 **Acknowledgements**

1214 We would like to thank Josh Randolph for maintenance and assistance with animal husbandry and
1215 handling. We thank Rajesh Gupta for his preliminary contributions to immunohistochemistry
1216 staining. We thank Veronica Obregon-Perko for her assistance with spectral flow cytometry panel
1217 design. We also thank Laura Volpicelli-Daly, Charlotte Brzozowski and Marissa Menard for their
1218 contribution of mouse α-syn PFFs for our studies. Lastly, we would like to thank Warren Hirst,
1219 Lucas Hampton and Karen Eskow-Jaunarajs for their input and guidance during the development
1220 of this project. We thank the UAB Comprehensive Flow Cytometry Core for their assistance with
1221 flow cytometry experiments. The core is supported by the Center for AIDS Research, AI027767,

The O'Neal Comprehensive Cancer Center, CA013148 and Shared instrument grant S10OD032296. Experimental design figures were generated using BioRender. This work was supported in whole by Aligning Science Across Parkinson's (Grant# ASUB00000984) through the Michael J. Fox Foundation for Parkinson's Research (MJFF). For the purposes of open access, the author has applied a CC BY public copyright license to all Author Accepted Manuscripts arising from this submission.

Author's contributions

JMW and ASH designed the study, experiments, and wrote the manuscript. JMW was responsible for planning and performing all stereotaxic surgeries. JMW, YTY, ATM, NJCS, WJW and AZ contributed towards tissue collection and executing flow cytometry experiments. TAY, WJS, KS and JMW performed all ELISA and immunoblotting experiments and analysis. JMW, NM and ACS conducted IHC stains. JMW manually assessed NeuN+ neuronal loss via unbiased stereology. AZ manually assessed Th+ neuronal loss via stereology. NHC, LFL, PNM, KMG and JHH planned, conducted and analyzed dendritic spine morphology counts. FPM and IS developed and optimized the AAV double-mutant tau vector. JMW and ASH drafted and constructed the manuscript and figures. FPM, JHK and DJT provided feedback on study design and edits to the manuscript. All authors read and approved the final manuscript.

Competing interests

The authors have no competing interests.

Extended Data Figures

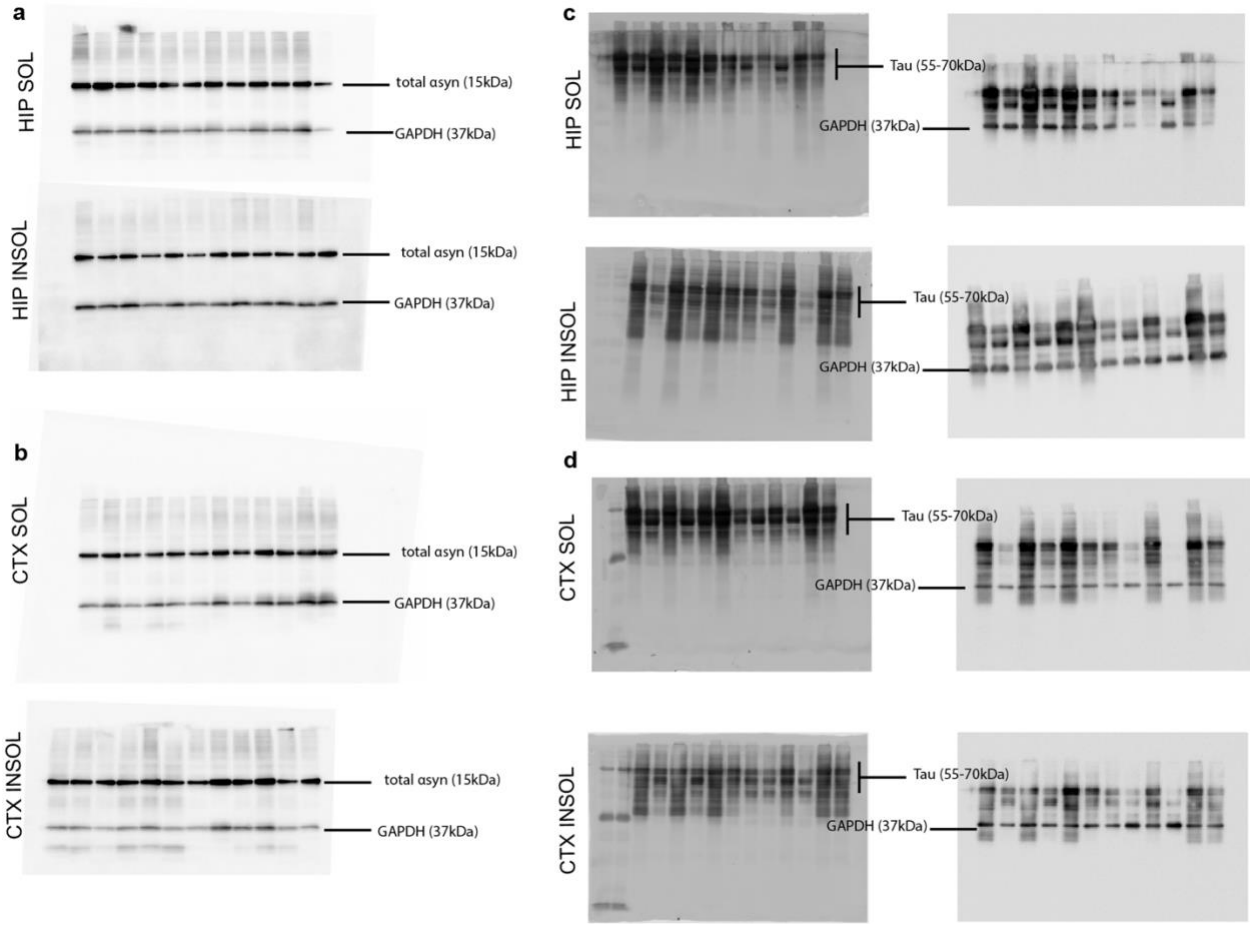

Extended Data Figure 1. Uncropped western blot images corresponding to Figure 1. (a,b) Blots probed for total α-syn and GAPDH from Triton-X100 soluble and insoluble (a) hippocampus and (b) cortex samples from co-pathology and single pathology animals. Blots probed for total tau and GAPDH from Triton-X100 soluble and insoluble (c) hippocampus and (d) cortex samples from co-pathology and single pathology animals. For c and d, the same membrane was probed sequentially for total tau and subsequently for GAPDH as a loading control.

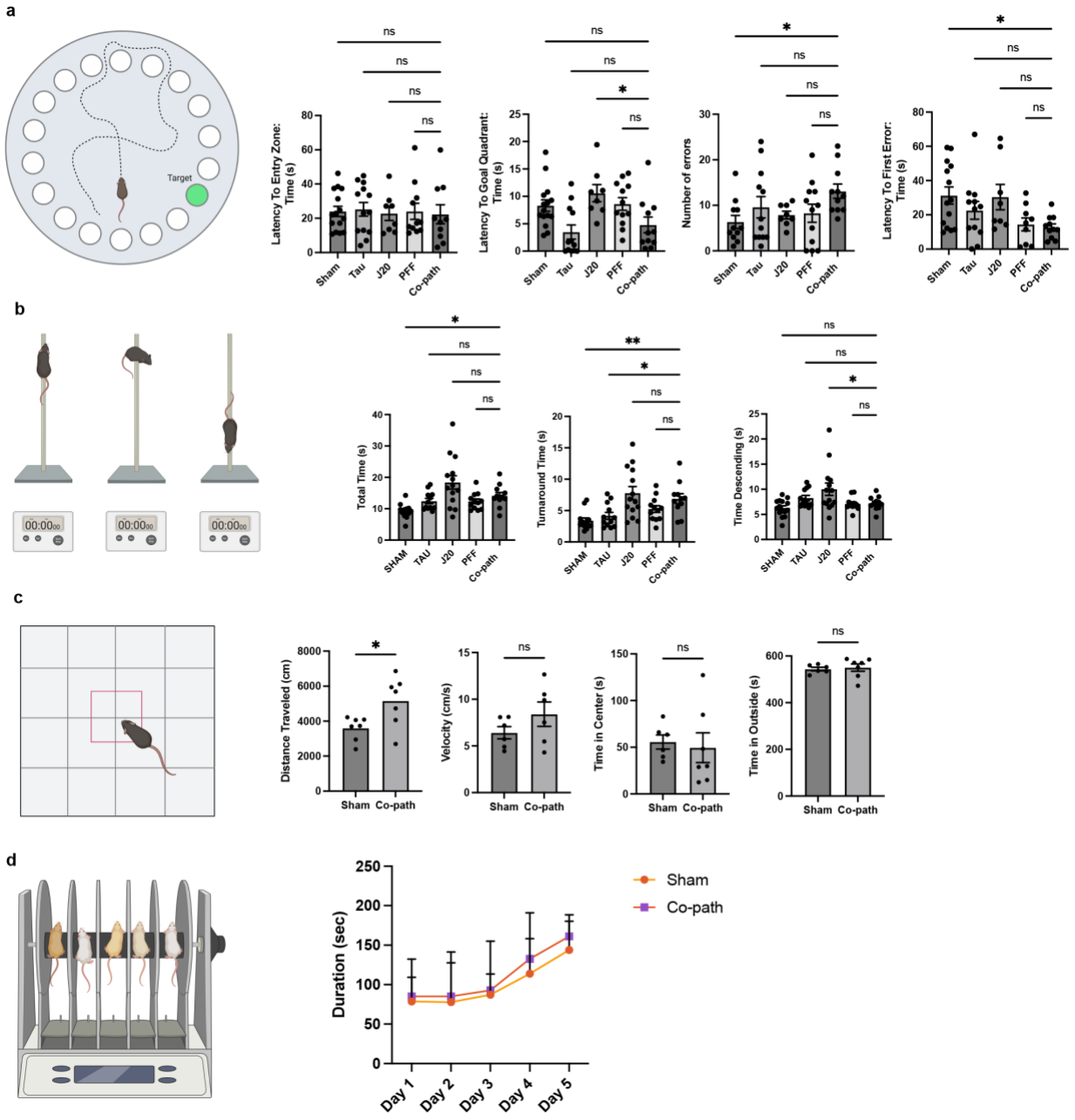

Extended Data Figure 2. A series of behavioral tests were conducted on co-pathology and single pathology animals. (a) Quantification of latency to entry zone, to goal quadrant, to first error and the total number of errors analyzed from Barnes maze test. (b) Measures of total time, turnaround time and time descending on the pole test. (c) distance travelled, velocity, time in center and time in outside are depicted from open field test. (d) Total duration of animals on rotarod platform

across 5 days of testing. One-way ANOVA with post hoc for significance. Mean values +/- SEM are plotted. ns = no significance, *p<0.05, **p<0.01, ***p<0.005. n=8-10 animals per group, both males and females used.

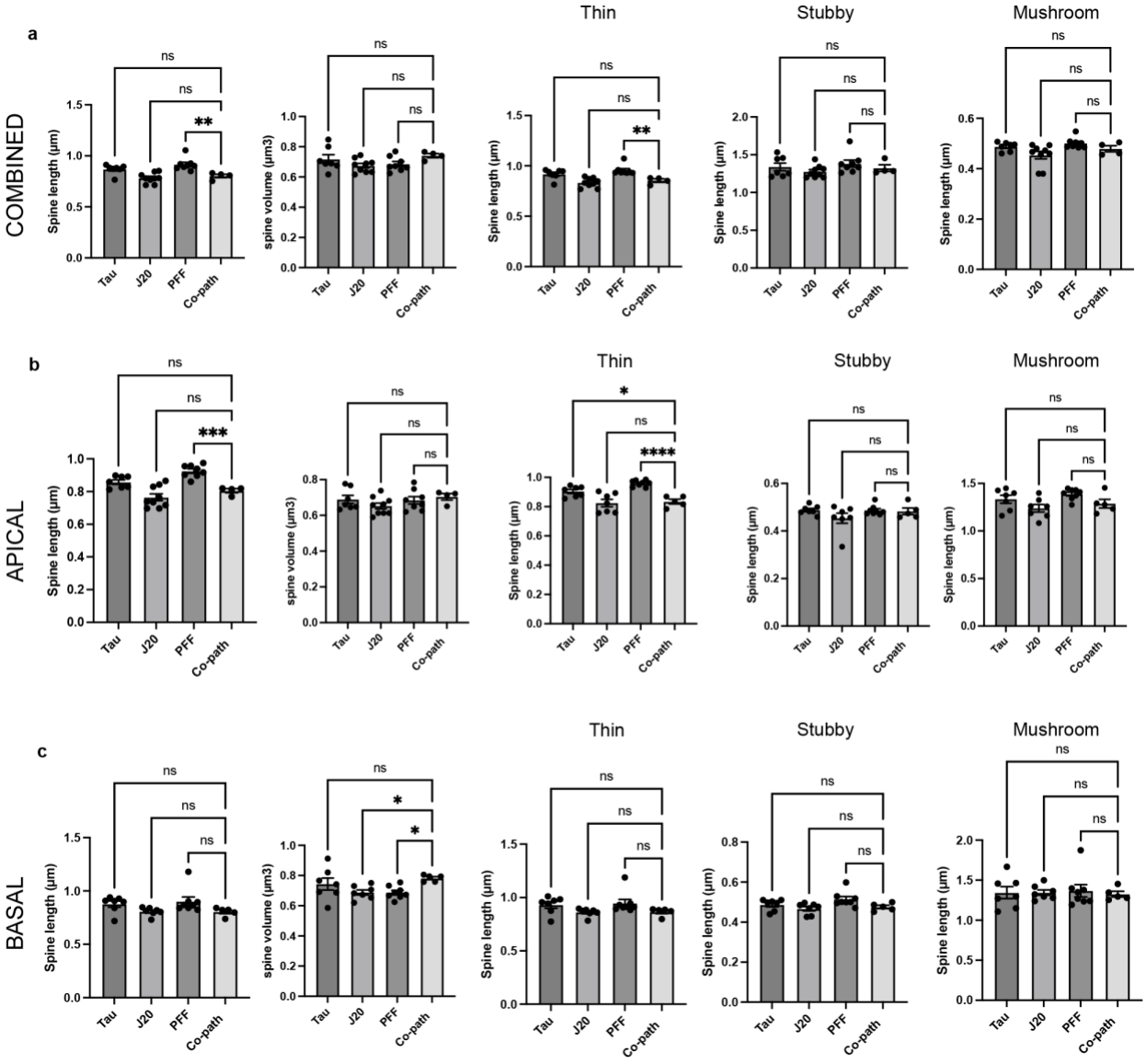

Extended Data Figure 3. Dendritic spine morphology was assessed in the CA1 region of hippocampus on pyramidal neurons and measures of total spine length and spine volume for all spines and for thin, stubby and mushroom subgroups are plotted from (a) combined (both apical

1271 and basal), (b) apical only or (c) basal only dendrites. One-way ANOVA with post hoc for
1272 significance. Mean values +/- SEM are plotted. ns = no significance, *$p<0.05$, **$p<0.01$,
1273 ***$p<0.005$. n=8-10 animals per group, both males and females used.
1274

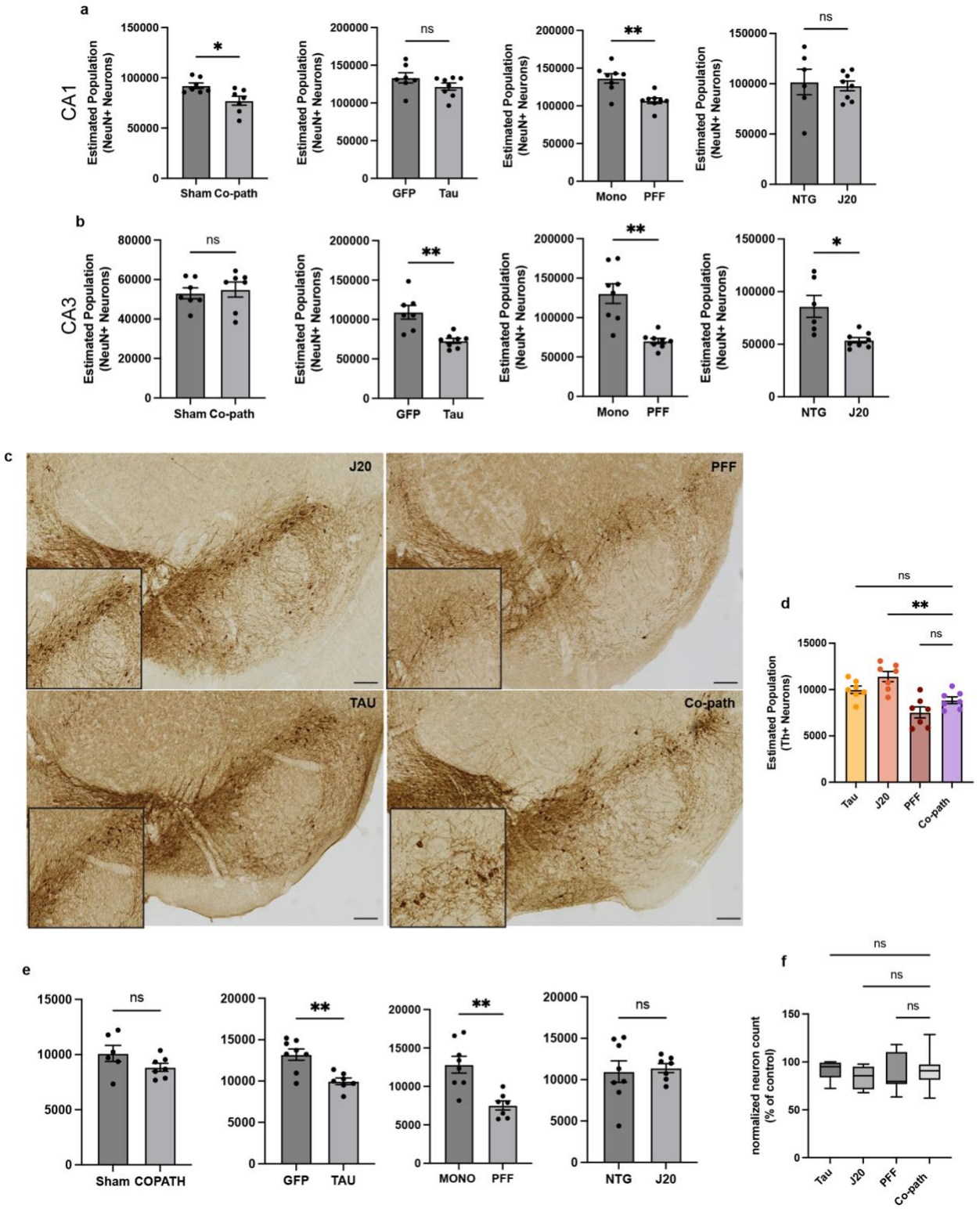

1275

1276 **Extended Data Figure 4.** Unbiased stereology was used to assess for neuronal loss in the

1277 hippocampus and SNpc. (a,b) Estimated population of NeuN+ neurons of co-pathology and single

1278 pathology CA1 or CA3 compared to their individual controls. (c) TH+ neurons (brown) in the
1279 SNpc of single pathology and co-pathology brains. (d) Unbiased stereology was used to quantify
1280 the number of TH+ neurons in the SNpc in the co-pathology mouse model compared to Tau, J20
1281 and PFF single pathology brains. All images taken at 20X. Scale bars = 100µm. One-way ANOVA
1282 with post hoc for significance. Mean values +/- SEM are plotted. Ns = no significance, **$p<0.01$,
1283 ***$p<0.005$, ****$p<0.0001$. n=7-8 animals per group, both males and females used.
1284

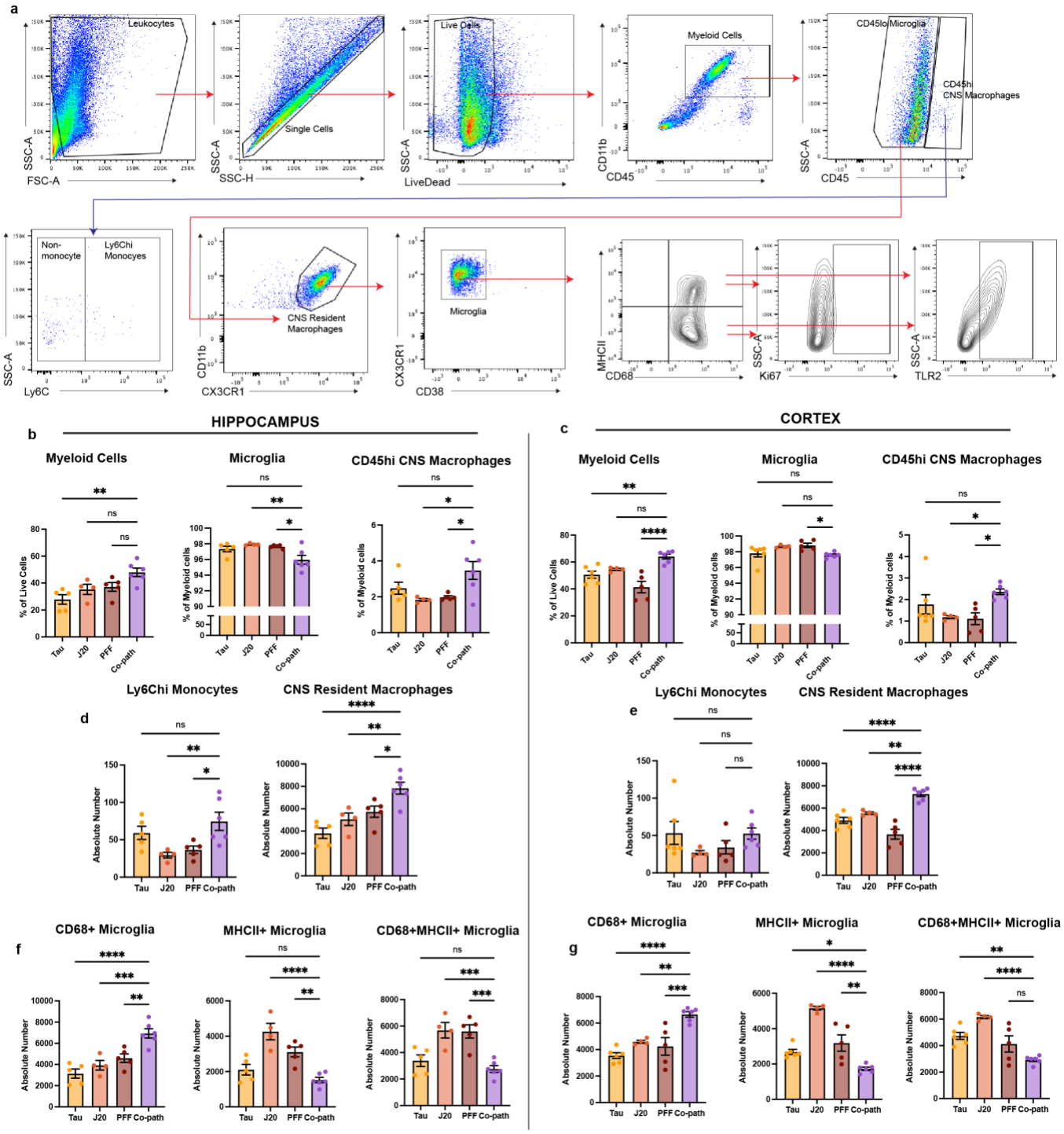

1285

1286 **Extended Data Figure 5.** (a) Gating strategy for flow cytometry analysis of microglia. (b)

1287 Quantification of proportion of myeloid cells, microglia and infiltrating monocytes/CNS resident

1288 macrophages in the co-pathology model hippocampus and (c) cortex compared to single pathology

1289 brains. (d,e) absolute number of CD68+ microglia, MHCII+ microglia and MHCII+CD68+
1290 microglia in the hippocampus and cortex of single pathology and co-pathology brains. Analyzed
1291 using One-way ANOVA. Mean values +/- SEM are plotted. *$p<0.05$, **$p<0.01$, ***$p<0.005$. n=5-
1292 6/group, with two brain regions pooled per sampled, both males and females included in analysis.
1293

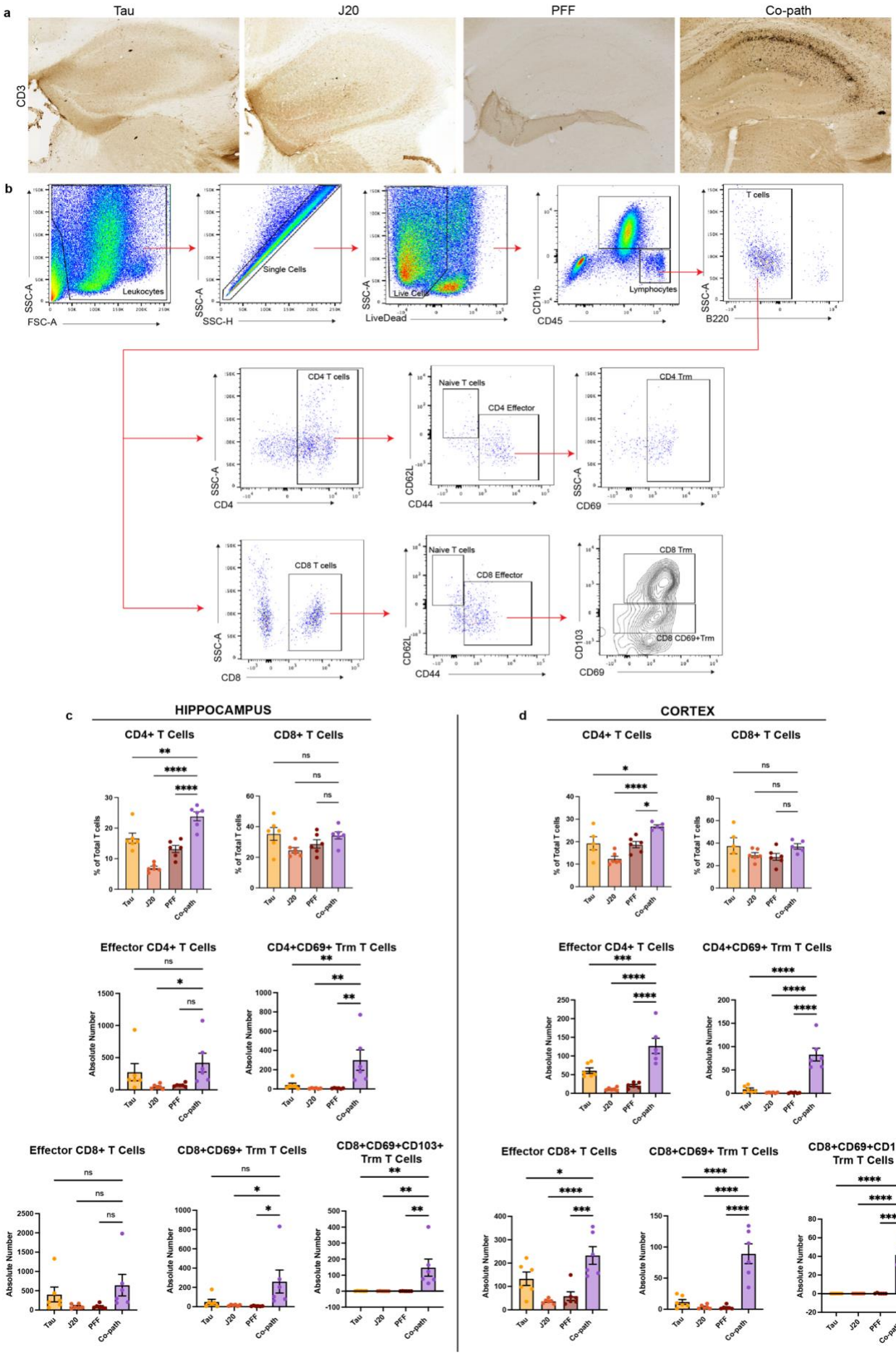
a
Tau
J20
PFF
Co-path
CD3
b
Leukocytes
Single Cells
Live Cells
Lymphocytes
T cells
SSC-A
FSC-A
SSC-H
LiveDead
CD11b
CD45
B220
CD4 T cells
Naive T cells
CD4 Effector
CD4 Trm
CD4
CD44
CD62L
CD69
CD8 T cells
CD8 Effector
CD8 Trm
CD8 CD69+Trm
CD8
CD103
c
HIPPOCAMPUS
CD4+ T Cells
CD8+ T Cells
Effector CD4+ T Cells
CD4+CD69+ Trm T Cells
Effector CD8+ T Cells
CD8+CD69+ Trm T Cells
CD8+CD69+CD103+ Trm T Cells
% of Total T cells
Absolute Number
d
CORTEX
CD4+ T Cells
CD8+ T Cells
Effector CD4+ T Cells
CD4+CD69+ Trm T Cells
Effector CD8+ T Cells
CD8+CD69+ Trm T Cells
CD8+CD69+CD103+ Trm T Cells
% of Total T cells
Absolute Number
Tau
J20
PFF
Co-path

1295 **Extended Data Figure 6.** (a) Representative images showing CD3+ staining (nickel) from Tau,
1296 J20, PFF and co-pathology brains. (b) Gating strategy for flow cytometry analysis of T cells. (c)
1297 Quantification from flow cytometry of proportion of CD4 and CD8 T cells, and absolute number
1298 of effector CD4 and CD8 T cells, and Trm T cells in the hippocampus and (d) cortex. Analyzed
1299 using One-way ANOVA. Mean values +/- SEM are plotted. *$p<0.05$, **$p<0.01$, ***$p<0.005$. n=5-
1300 6/group, with two brain regions pooled per sampled, both males and females included in analysis.
1301
1302
1303